https://doi.org/10.5194/egusphere-2026-1636
Preprint. Discussion started: 8 April 2026

Climatic Impacts of the 536 and 540 CE Volcanic Eruptions Simulated with COSMO-CLM over the Middle East and Africa

Eva Hartmann[1], Sebastian Wagner[2], Jürg Luterbacher[1], and Elena Xoplaki[3]

[1]Department of Geography, Climatology, Climate Dynamics and Climate Change, Justus-Liebig University, Giessen, Germany
[2]Helmholtz-Zentrum Hereon, Geesthacht, Germany
[3]CMCC Foundation - Euro-Mediterranean Center on Climate Change, Bologna, Italy

Correspondence: Eva Hartmann (eva.hartmann@geogr.uni-giessen.de)

Abstract. The past 2500 years were marked by major historical developments across the eastern Mediterranean, the Middle East, the Arabian Peninsula, and the Nile Basin from Lake Victoria to the Nile Delta. Modeling efforts by both the global and regional climate modeling communities remain limited in this region. Here, we address this gap by presenting the first transient regional climate simulation for the area spanning 2350 years, from 500 BCE to 1850 CE, using the COSMO-CLM model. The simulation reveals an exceptionally pronounced climatic response to the consecutive volcanic eruptions of 536 and 540 CE, which motivated an additional century-long ensemble experiment to investigate this interval in greater detail. The eruptions produce marked surface cooling through reduced incoming solar radiation and are accompanied by large-scale circulation anomalies. In the simulation, widespread cooling persists until around 550 CE, with boreal summers showing the strongest anomalies during the first two to three years after the eruptions. Precipitation responses display strong regional contrasts: anomalously wet conditions occur over the Mediterranean, the Middle East, and Southeast Africa, particularly during the climatologically dry Northern Hemisphere summer season, whereas the Sahara, the Arabian Peninsula, Central Africa, and Northeast Africa experience concurrent dryness concentrated in their respective rainy seasons. The most severe climatic anomalies occur within the first one to two years after the eruptions and gradually weaken over the following years.

1 Introduction

The climate of the past 2000 years has been studied extensively, but substantial uncertainties remain regarding the magnitude, spatial expression, and temporal evolution of climate variability, extremes, and trends across regions, seasons, and time scales (2k Consortium', 2013; Christiansen and Ljungqvist, 2017; Neukom et al., 2019; Turney et al., 2019). However, the sixth century CE stands is widely recognized as a particularly anomalous period within the past 2000 years, commonly linked to its cluster of major volcanic eruptions, especially those of 536 and 540 CE (Sigl et al., 2015; Toohey et al., 2016; Büntgen et al., 2020; Neukom et al., 2019). Such eruptions are a major source of abrupt, externally forced climate variability on annual to multiannual timescales because sulfur injected into the stratosphere forms sulfate aerosols that reduce incoming shortwave radiation and thereby perturb atmospheric circulation, near-surface temperatures, and hydroclimate (Robock, 2000). Accordingly, the mid-sixth-century eruption cluster represents an especially valuable case for investigation, because its precisely dated

https://doi.org/10.5194/egusphere-2026-1636
Preprint. Discussion started: 8 April 2026

forcing signal in ice-core-based reconstructions can be directly evaluated against independently dated climate proxy records and contemporaneous historical evidence (Sigl et al., 2015; Toohey et al., 2016). Existing evidence indicates an exceptional cooling anomaly in the years after 536 CE and motivate the hypothesis of a sustained cooling interval in parts of the Northern Hemisphere during the sixth and seventh centuries (Büntgen et al., 2016; Helama et al., 2018). However, the magnitude, persistence, and spatial expression of the response were likely not uniform because circulation-related and hydroclimatic anomalies can differ substantially across regions and seasons despite identical external forcing (Swingedouw et al., 2017; Zanchettin et al., 2019).

In parts of the Northern Hemisphere, the concurrent sixth-century eruptions initiated a prolonged period of pronounced cooling, which in turn led to social disruption, famine, and outbreaks of epidemic disease in many regions (Gibbons, 2018; Newfield, 2018; Gunn, 2000; Helama et al., 2018; Luterbacher et al., 2020; Peregrine, 2020). Recent syntheses emphasize that societal impacts were highly heterogeneous across regions and shaped by differing political and economical contexts, and that causal interaction therefore require regionally specific climate evidence alongside careful historical analysis (Luterbacher et al., 2020; Newfield, 2018; Peregrine, 2020). This period is commonly referred to as Late Antique Little Ice Age (LALIA) (Büntgen et al., 2016). Notably, the onset of the Justinianic Plague in the Mediterranean coincided with the early part of this interval (Newfield, 2016; Luterbacher et al., 2020). Together, these considerations highlight the need to better constrain the spatiotemporal climate response across the Mediterranean, the Middle East, and Africa, where seasonality and hydroclimate variability were central to both environmental conditions and societal vulnerability. In this context, the Mediterranean and its wider connected regions are particularly important settings for investigating the climatic consequences of the mid-sixth-century eruptions.

The Mediterranean Sea, its surrounding regions, and the Nile River basin are of outstanding historical interest, having been home to great civilizations such as Ancient Egypt (Wilson, 1956), Ancient Greece (Sallares, 1991), and Ancient Rome (Feldman, 1991). Climatic variability has long been considered one of the factors interacting with historical and societal developments across this broader region (Crowley and North, 1988; Holmgren et al., 2016; Izdebski et al., 2016). However, for the sixth century in particular, the availability of spatially, seasonally resolved climate information remains uneven, especially for precipitation and circulation-related mechanisms that are critical for water balance and agricultural risk (Xoplaki et al., 2021). Existing evidence derived from both natural proxy records, which are indirect measurements of past climatic conditions (Ingram et al., 1985), and historical sources such as reports, logbooks, and diaries or indirect documentary proxy data (Brázdil et al., 2005; Burgdorf, 2022; Xoplaki et al., 2018, 2021), all of which extend climate information beyond the instrumental period. At the same time, proxy archives differ in their climatic sensitivity, reproducibility, local availability, temporal continuity, and dating uncertainties, which complicates comparisons and the reconstruction of coherent regional patterns (Mann, 2002; Xoplaki, 2002; Thornes et al., 2009; Bradley, 2014; Smerdon et al., 2017; Luterbacher et al., 2012; Conedera et al., 2009; Fairbanks et al., 1997; Conroy et al., 2014; Felis and Pätzold, 2003). For this purpose, gridded climate reconstructions provide a more suitable basis for comparing different climatic variables over the last 2000 years, drawing in particular on tree ring data at European and broader Northern Hemisphere scales (Cook et al., 2015; Luterbacher et al., 2002, 2004; Pauling et al., 2006; Valler et al., 2024). Based on such data sources, the climate of the Late Antiquity has, for example, been examined by Xoplaki et al. (2021). Across the literature, the climate response to the large volcanic eruptions in the sixth century is more visible

https://doi.org/10.5194/egusphere-2026-1636
Preprint. Discussion started: 8 April 2026

as a shift in seasonality and hydroclimate than as an altered annual mean temperature in the broader Mediterranean region (Mangini et al., 2005; Helama et al., 2017b; Riechelmann and Gouw-Bouman, 2019; Izdebski and Mulryan, 2019; Degroot et al., 2021). This highlights the importance of analyzing monthly to seasonal anomalies and circulation changes in addition to annual means. At the same time, high-resolution data covering larger regions remain scarce (Helama et al., 2017a).

This highlights the need for a process-based understanding of the underlying climate dynamics. Global climate simulations with modern Earth System Models support the understanding of physical mechanisms behind past climate changes. By representing large-scale atmospheric and oceanic circulation, as well as interactions among Earth system components, they help to interpret proxy data and the reconstructions derived from it. Simulations confirm the onset of cooling after 536 CE relative to earlier centuries of the Common Era (Shi et al., 2022; Büntgen et al., 2016; Büntgen et al., 2020). However, discrepancies remain among data sources regarding the timing and regional extent of this cooling. A substantial gap also persists between local proxy evidence and global simulations, particularly for hydroclimate, where internal variability and regional circulation responses can dominate and mask externally forced signals (Xoplaki et al., 2018, 2021). Dynamical downscaling with regional climate models offers an established pathway to bridge this scale gap by providing higher resolution climate fields that can be analyzed in a process-based way and compared more directly with regionally distributed evidence. Regional analyses using dynamically downscaled simulations have, for example, already been applied to parts of Europe in related contexts (van Dijk et al., 2022, 2023). Comparable high-resolution transient regional simulations remain scarce for the Mediterranean, the Middle East, and Northeast Africa during the first millennium CE, limiting process-based assessment of volcanic impacts on seasonality, hydroclimate, and circulation in this historically important domain.

To help bridge the gap between local proxy evidence and global climate simulations, we here make use of results from a transient regional climate simulation with an adjusted version of COSMO-CLM covering the period from 500 BCE to 1850 CE. This paleo-version of COSMO-CLM incorporates CMIP6-compliant external forcings, including volcanic, orbital, solar, greenhouse-gas, and land-use, which are applied not only to the driving global model MPI-ESM but also directly to the regional model Hartmann et al. (2025). To strengthen the robustness of the results and to reduce uncertainties arising from internal variability, two simulations with different initial conditions were carried out, providing plausible realizations of sixth-century climate evolution. The closely spaced eruptions of 536 and 540 CE provide a particularly stringent test case because strong external forcing coincides with potentially circulation-mediated and regionally diverse responses.

Transient ensemble simulations in paleoclimate research remain rare due to their high computational costs. Where only a single realization is available, robustness is difficult to assess, especially for precipitation and atmospheric circulation. At the global scale, ensembles forced with the same set of external forcings typically produce very similar near-surface temperatures, whereas results can diverge more at regional-to-local scales (Goosse et al., 2005). This is particularly relevant for hydroclimate, where signal-to-noise ratios are often lower, and the need for multiple realizations and explicit regional analysis is therefore even stronger. A key question in this context is which parts of the temperature, precipitation, and circulation response to the sixth-century eruptions remain robust across realizations, and how these responses vary across contrasting climatic zones within the domain. Addressing this requires a study region that includes both the margin of the Mediterranean storm track and adjacent subtropical to tropical regimes. Across these zones, circulation patterns and moisture pathways differ substantially, so

https://doi.org/10.5194/egusphere-2026-1636
Preprint. Discussion started: 8 April 2026

volcanic forcing may affect hydroclimate in contrasting ways.

Our new simulations cover a large part of the Eastern Mediterranean, the Middle East, and Northeast Africa. To account for the diversity of climatic conditions across this domain, we adopt the IPCC reference regions for the subcontinental analysis of climate model data (Iturbide et al., 2020). We investigate regional impacts on 2m temperature and precipitation at annual, seasonal, and monthly timescales, and we analyze circulation changes to interpret the regional responses. By providing a spatially explicit and seasonally resolved characterization of the anomalies associated with the 536 and 540 CE eruptions and their immediate aftermath, this study contributes high-resolution process-based evidence for a historically important region where such information remains limited. Details on the models, the domain, and the general circulation within the study area are presented in the Data and Methods section. The following sections present the results together with their interpretation, followed by the conclusions and an outlook.

2 Data and Methods

2.1 Global Climate Model and Forcing Data

We analyze downscaled regional climate simulations over the eastern Mediterranean, the Middle East, and Africa to investigate climate variability over the past 2500 years in a process-based framework and at a regional scale. The downscaling setup is based on a global simulation with the MPI-ESM (Giorgetta et al., 2013). It follows the CMIP6-protocol for PMIP4 past1000 simulations by Jungclaus et al. (2017). The temporal output of the global simulation is adapted to the requirements of the regional climate model COSMO CLM by providing 6-hourly fields.

The MPI-ESM consists of the coupled general circulation models for the atmosphere ECHAM6 (Stevens et al., 2013), the ocean MPIOM (Jungclaus et al., 2013), subsystem models for land and vegetation JSBACH (Reick et al., 2013; Schneck et al., 2013), and for the marine biogeochemistry HAMOCC5 (Ilyina et al., 2013). The atmospheric and vegetation variables are needed as input at the lateral boundaries and for surface conditions for the regional climate simulation. The spatial resolution of the global simulation is 1.875°, which is approximately 200 km (T63). Two realizations are available with identical external forcings but different initial conditions, enabling an assessment of robustness against internal variability at the regional scale.

External forcings are implemented following the PMIP4 past1000 framework (Jungclaus et al., 2017) and include orbital forcing (Berger, 1978), solar forcing (Jungclaus et al., 2017), volcanic forcing (Sigl et al., 2015; Toohey and Sigl, 2017), greenhouse gas concentrations (Meinshausen et al., 2017), and changes in land use. These forcings are applied in the driving MPI ESM and, for consistency, are also implemented directly in the regional model as described below.

2.2 Regional Climate Model and Experimental Setup

For our target region we performed numerical simulations with the regional climate model COSMO-CLM (Rockel et al., 2008) based on the MPI-ESM. COSMO-CLM is the model of the COnsortium for Small-scale MOdelling (COSMO) in CLimate

https://doi.org/10.5194/egusphere-2026-1636
Preprint. Discussion started: 8 April 2026

	period	global model horizontal resolution	regional model horizontal resolution	forcings
r1	500 BCE - 1850 CE	MPI-ESM 1.875°	COSMO-CLM 0.44°	volcanic, orbital, solar, greenhouse gas, land-use
r2	500 CE - 700 CE	MPI-ESM 1.875°	COSMO-CLM 0.44°	volcanic, orbital, solar, greenhouse gas, land-use

Table 1. List of simulations used in this article.

Mode (Baldauf et al., 2011; Rockel et al., 2008). In the present study, the COSMO model version 5.0 with CLM version 16 (COSMO-CLM $-$ $v5.0\_clm16$) is used. The interpolation of the MPI-ESM forcing data onto the regional model grid is performed with INT2LM in version 2.05 with CLM version 1 (INT2LM $-$ $v2.05\_clm1$) (Schättler and Blahak, 2017). The time integration uses the two-time-level Runge-Kutta scheme (Jameson et al., 1981), and the model time step is 25 seconds. For the regional simulations, the convection parameterization based on the Tiedtke scheme (Tiedtke, 1988) is used. The representation of albedo and aerosols is important in this region and parameters are set according to values provided by Bucchignani et al. (2016). The land surface model is TERRA-ML (Doms et al., 2011; Schulz et al., 2016). The external lower-boundary data set is created from MPI-ESM output on a monthly basis. The same PMIP4-compliant external forcings as used for MPI-ESM are implemented in COSMO-CLM as described in Hartmann et al. (2025).

The regional simulations are carried out on a native rotated geographical grid with a mesh grid size of 0.44° ($\sim$ 50 km). We performed one transient simulation for the complete period from 500 BCE to 1850 CE across the entire domain at the same resolution (first realization, r1, Table 1). This simulation is used to show the long-term evolution of temperature and precipitation over the entire simulation period. As a reference for all anomalies calculated in the following results, we took the period from 1 CE to 1850 CE of this transient simulation. The reconstructions selected for PMIP4 past1000 were officially extended to this period for past2k experiments (Jungclaus et al., 2017). We also performed simulations prior to this period, but do not use this as a reference, as the reconstructions are not recommended for BCE. Furthermore, the period 1–1850 CE proved to be representative of the entire pre-industrial Common Era (van Dijk et al., 2022). Since the sixth century exhibits the greatest consistency across individual subregions in terms of significant anomalies throughout the entire simulation, we conducted a second model run (second realization, r2, Table 1) using exactly the same settings but with different initial conditions for both the global and regional models. The second realization is simulated for the period 500 to 700 CE. Together with the transient simulation for this exact period, this small ensemble of two simulations forms the basis for all detailed investigations into the effects of the volcanic eruptions in 536 and 540 CE. This approach allows us to more clearly distinguish the effects of external factors from the model's internal variability.

2.3 Simulation Domain with Subregions

The simulation domain spans approximately 4° to 60° East and 5° South to 49° North. It encompasses the Eastern Mediterranean, the Middle East, the Arabian Peninsula, and a large portion of the African continent, stretching from the Eastern

https://doi.org/10.5194/egusphere-2026-1636
Preprint. Discussion started: 8 April 2026

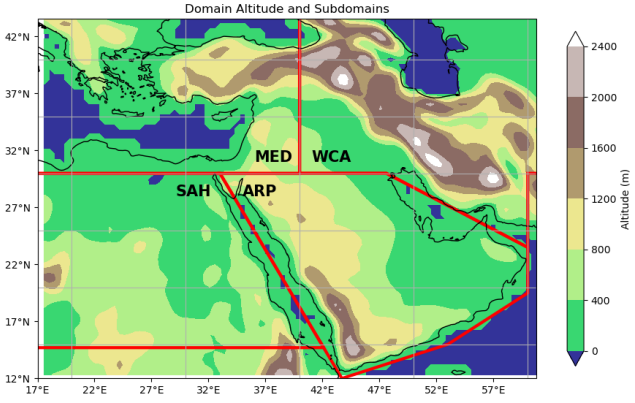

Figure 1. Simulation domain with topography divided into the seven sub-domains Mediterranean (MED), Western Central Asia (WCA), Sahara (SAH), Arabian Peninsula (ARP), Central Africa (CAF), North East Africa (NEAF), and South East Africa (SEAF).

Mediterranean coast, across the Sahara Desert and the tropical rainforest, to Lake Victoria (Figure 1). The domain was specifically chosen to include the Eastern Mediterranean and the Black Sea, as well as the entire Nile River basin and the Middle East. This region exhibits significant orographic diversity, encompassing coastal areas, one of the world's largest deserts, and major mountain ranges such as the Taurus, Caucasus, Zagros, and Ethiopian Highlands, as well as Mount Kilimanjaro. According to the Köppen-Geiger climate classification (Beck et al., 2023), it includes tropical rainforest to arid deserts and temperate to cold climates in the northernmost mountains.

Given the domain's large geographical extent and pronounced climatic contrasts, we subdivide it into seven subregions following the IPCC reference regions for subcontinental analysis (Iturbide et al., 2020). Those subregions should be understood as broadly defined diagnostic regions, not as internally homogeneous climate units. These include the Mediterranean (MED), encompassing its coastlines and adjacent areas, and Western Central Asia (WCA), which contains the domain's highest mountain ranges in the north. Two sub-domains are predominantly desert, the Sahara (SAH) and the Arabian Peninsula (ARP). Central Africa (CAF) is characterized by tropical rainforest, alongside monsoon or savanna climates. Northeast Africa (NEAF) exhibits a high degree of heterogeneity, spanning coastal zones, mountains, rainforest, and desert. Finally, Southeast Africa (SEAF), while the smallest subregion, also features coastal areas and mountains though less prominent than in NEAF, and encompasses a distinct set of climatic classifications. This regionalization provides a consistent basis for aggregating anomalies and comparing responses across contrasting climatic regimes within the same forced experiment. Nevertheless, it must not be neglected that the individual subregions exhibit significant geographical variability and differ greatly in terms of both hydroclimatic and

https://doi.org/10.5194/egusphere-2026-1636
Preprint. Discussion started: 8 April 2026

thermal conditions. This applies in particular to the highly heterogeneous WCA and NEAF subregions, as well as to the CAF subregion, which spans both hemispheres.

2.4 General Atmospheric Circulation

Besides the geographical and climatological differences, the subregions are also affected by very different general atmospheric circulation regimes, which vary between the seasons. Nicholson (2018) shows the general circulation for Africa in the boreal summer (July/August) and in the boreal winter (January). In winter, the MED and WCA domains are mainly influenced by the midlatitude westerlies, the North Atlantic Oscillation (NAO), the East Atlantic (EA), and the Scandinavian patterns (SCAND) (Ulbrich et al. (2012); Cullen et al. (2002); Mann (2002) and references therein). During summer, the MED climate is dominated by the Etesians, a strong northerly wind with the greatest influence on the Aegean Sea (Dafka et al., 2016). This wind pattern is influenced by the South Asian monsoon and amplified by the pronounced topography Tyrlis et al. (2013); Simpson et al. (2015). For the same reason, WCA is also dominated by northerly winds. The domains ARP and NEAF are mainly influenced by the Indian summer monsoon with strong winds from south-east to north-east. During summer this system is characterized by northerly winds in ARP (Attada et al., 2019) and southerly winds in the eastern part of NEAF, while the western part of NEAF and CAF are affected by the African monsoon, also with southerly winds (Camberlin, 1997; Nicholson, 2018). Because of the northernmost position of the Intertropical Convergence Zone (ITCZ) during boreal summer, the domain is divided into a northern and southern part relative to the ITCZ. During boreal winter, the ITCZ is located at its southernmost position. This means that SAH, ARP, NEAF, and SEAF are affected by northerly winds, and ARP and NEAF also by the Indian winter monsoon, with only moderate winds from east to southwest over the Indian Ocean. Only the CAF region is divided in the east-west direction.

The entire domain exhibits pronounced variability in precipitation regimes. It encompasses hyper-arid desert areas with near-zero rainfall, tropical rainforest zones characterized by consistently high precipitation throughout the year, and transitional regions featuring distinct unimodal or bimodal rainfall peaks depending on the location of the ITCZ. This strong seasonality and regime dependence motivate an analysis of temperature and precipitation responses on annual, seasonal, and monthly time scales, together with circulation diagnostics, in the subsequent sections.

3 Results

3.1 Transient Simulation from 500 BCE to 1850 CE

Figure 2 shows the annual (January to December) mean 2m temperature for the subregions (Figure 1) as anomalies with respect to the 1-1850 CE reference period together with the 30-year running mean. The climate of the simulated period from 500 BCE to 1850 CE is highly variable. Warm and cold, wet and dry periods alternate, with overlaps and deviations between the individual subregions. The overlap between the regions for the coldest years (blue bars in Figure 2) is highest in the years following major volcanic eruptions. Those are mainly the eruptions in 423 BCE, 44 BCE, 536/540 CE, 1257 CE, 1458 CE, and 1815 CE, which

https://doi.org/10.5194/egusphere-2026-1636
Preprint. Discussion started: 8 April 2026

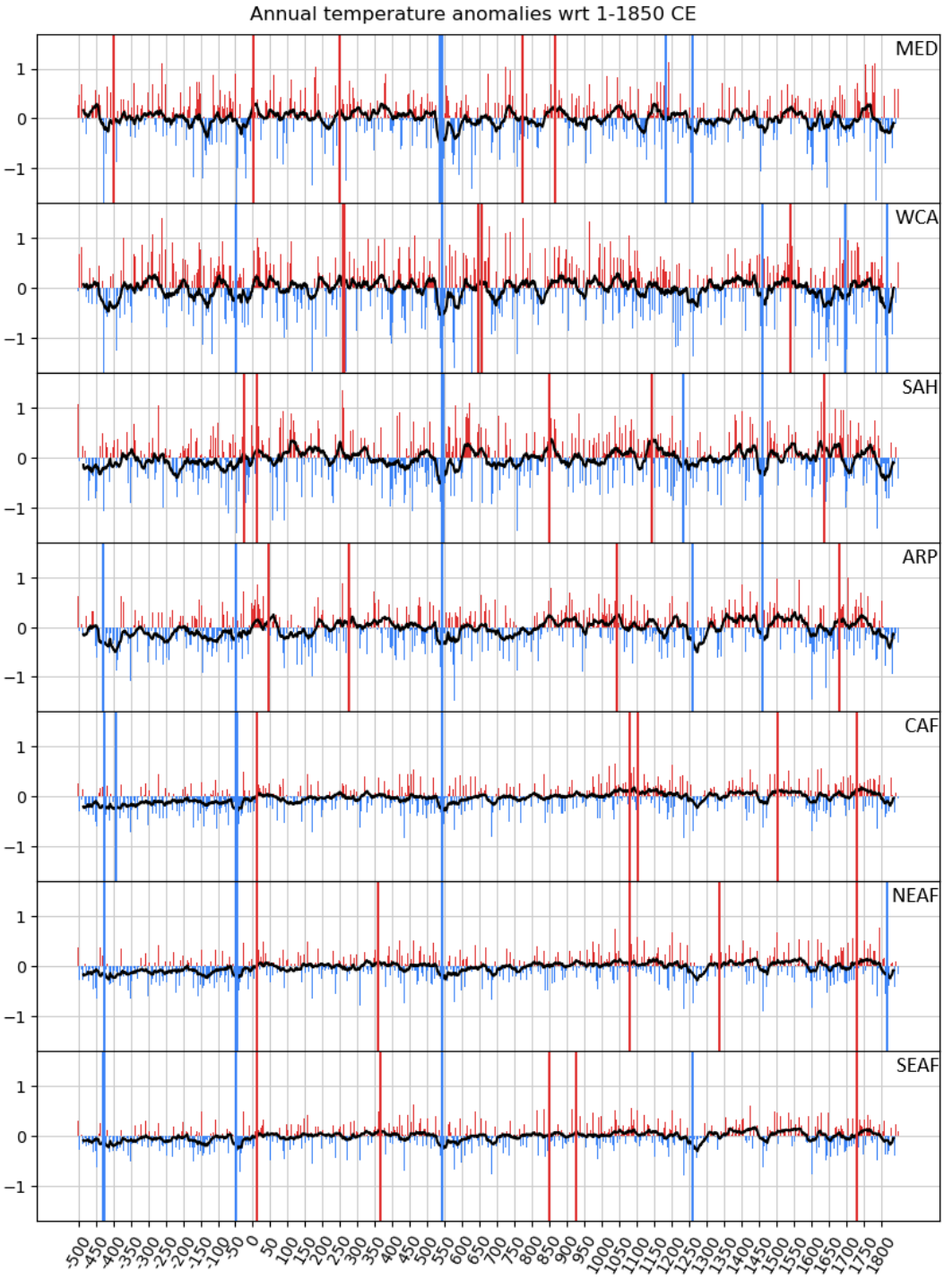

Figure 2. Temperature anomalies for the MED, WCA, SAH, ARP, CAF, NEAF, and SEAF regions wrt 1-1850 CE for the entire simulated period from 500 BCE to 1850 CE with the 5 warmest and coldest years highlighted as red and blue bars, respectively, and the 30-year running mean in black.

https://doi.org/10.5194/egusphere-2026-1636
Preprint. Discussion started: 8 April 2026

are, according to Toohey and Sigl (2017), the most severe eruptions of the past 2500 years. The 423 BCE eruption can be seen in the coldest years of the more southern subregions which are ARP, CAF, NEAF, and SEAF. The same applies to the 44 BCE eruption, which is additionally one of the five coldest years in WCA. The Samalas eruption in 1257 CE causes one of the coldest years in MED, ARP, and SEAF, while the 1458 CE eruption stands out particularly in WCA, SAH, and ARP, that is, in the regions with the highest desert fraction. The Tambora eruption in 1815 CE coincides with one of the coldest years in WCA and NEAF. Overall, volcanic eruptions account for most of the coldest years in the simulation, with a high degree of agreement among the subregions. The agreement for the warmest years (red bars in Figure 2) is not as clear, but there are similarities for unknown reasons around 0, around 250 CE, 1050 CE, and 1700 CE.

On a seasonal scale, the results are comparable and are therefore presented in the Appendix. In JJA (Figure A1), the agreement for cooling after the two BCE volcanic eruptions is higher and almost all subregions agree on a very warm year at the beginning of the Common Era and around 1730 CE. For DJF temperatures (Figure A3), the results are essentially consistent, but less uniform.

As we have a long timeseries of 2350 years we do not want to focus only on single years, but also examine the most extreme decadal to multidecadal periods. Therefore, we show the coldest and warmest, as well as wettest and driest 10-, 15-, 20-, 25-, and 30-years periods of the simulation in Table 2. For the coldest periods MED, WCA, and SAH all agree for periods around the eruptions in 536/540 CE. All subregions agree on the coldest 15-year period between 536 and 550 CE. We therefore focus on this period in the following subsections. Other cold periods are around the eruptions in 44 BCE, and 1257 CE, and around 400 BCE in ARP. The warmest periods largely differ between the subregions and with the length of the periods reviewed, but they all occur at least partly within the Common Era. For JJA (Figure A1), the variety of coldest and warmest periods is higher between the different subregions. During the Northern Hemisphere summer, only the MED, WCA, and CAF agree that the period after the 536/540 CE eruptions is the coldest in the time series. In DJF, it is the coldest 15-years period in all subregions except for ARP, where only the 10-years after the eruption in 536 CE constitute the coldest period. In MED, WCA, and SAH, it is the coldest period for all considered time ranges. No comparable pattern emerges for the warmest periods, which are distributed across the entire simulation period.

Figure 3 shows the annual total precipitation (January to December) for the subregions as anomalies with respect to the 1-1850 CE reference period together with the 30-year running mean. The five wettest years are marked with green bars and the five driest years with ochre bars. The differences between the regions are more distinct than for the temperature, and wet and dry years are widely distributed. In general, the first 1000 years of the simulation appear to have more wet years, which is most visible in SAH and ARP with running means remaining above the reference period. The first and second centuries CE are wetter in the more southerly subregions CAF, NEAF, and SEAF. The seasonal timeseries of precipitation (Figure A2 and Figure A4) show variability similar to that of the annual timeseries and are therefore also shown in the Appendix. JJA is the wet season in SAH, ARP, CAF, and NEAF under the influence of the ITCZ and the dry season in the northern (MED, WCA) and the southern (SEAF) part of the domain. In particular, the SAH subregion shows more JJA precipitation from 500 BCE to 500 CE. DJF, in contrast, is very dry in SAH, ARP, and NEAF, while CAF shows similar precipitation amounts to those in JJA. The subregion CAF spans the complete latitudes of NEAF and SEAF, meaning it represents the heterogeneous hydroclimate of

https://doi.org/10.5194/egusphere-2026-1636
Preprint. Discussion started: 8 April 2026

		10-years	15-years	20-years	25-years	30-years
cold	MED	**536 - 546**	**535 - 550**	**533 - 553**	**528 - 553**	**522 - 552**
	WCA	**536 - 546**	**535 - 550**	**533 - 553**	**535 - 560**	**522 - 552**
	SAH	**539 - 549**	**535 - 550**	**531 - 551**	**525 - 550**	**521 - 551**
	ARP	**536 - 546**	**535 - 550**	-406 - -386	-405 - -380	1257 - 1287
	CAF	-48 - -38	**536 - 551**	**538 - 558**	**536 - 561**	**530 - 560**
	NEAF	-48 - -38	**536 - 55**1	**538 - 558**	1256 - 1281	1257 - 1287
	SEAF	-48 - -38	**536 - 551**	-48 - -28	1257 - 1282	1258 - 1288
warm	MED	376 - 386	370 - 385	1746 - 1766	-6 - 19	-5 - 25
	WCA	964 - 974	246 - 261	1 - 21	1032 - 1057	1029 - 1059
	SAH	609 - 619	605 - 620	606 - 626	842 - 867	840 - 870
	ARP	273 - 283	370 - 385	371 - 391	1421 - 1446	1537 - 1567
	CAF	317 - 327	311 - 326	1076 - 1096	1077 - 1102	1728 - 1758
	NEAF	1627 - 1637	804 - 819	1142 - 1162	1422 - 1447	1423 - 1453
	SEAF	1627 - 1637	1421 - 1436	1417 - 1437	1422 - 1447	1423 - 1453
wet	MED	-144 - -134	-147 - -132	760 - 780	-145 - -120	-148 - 118
	WCA	-421 - -411	-426 - -411	-423 - -403	-424 - -399	-423 - -393
	SAH	2 - 12	1 - 16	2 - 22	-368 - -343	-367 - -337
	ARP	-149 - -139	-148 - -133	-152 - -132	-487 - -462	-483 - -453
	CAF	105 - 115	99 - 114	99 - 119	92 - 117	84 - 114
	NEAF	-364 - -354	90 - 105	88 - 108	83 - 108	83 - 113
	SEAF	175 - 185	882 - 897	84 - 104	83 - 108	76 - 106
dry	MED	592 - 602	376 - 391	1610 - 1630	1604 - 1629	362 - 392
	WCA	-276 - -266	1265 - 1280	-278 - -258	-279 - -254	766 - 796
	SAH	**536 - 546**	1696 - 1711	1704 - 1724	1694 - 1719	1694 - 1724
	ARP	1250 - 1260	1703 - 1718	1700 - 1720	1694 - 1719	1691 - 1721
	CAF	1254 - 1264	1252 - 1267	1175 - 1195	1057 - 1082	1671 - 1701
	NEAF	1780 - 1790	1779 - 1794	1780 - 1800	1780 - 1805	1780 - 1810
	SEAF	-315 - -305	1795 - 1810	1798 - 1818	1796 - 1821	1796 - 1826

Table 2. Coldest, warmest, wettest, and driest periods of 10, 15, 20, 25, and 30 years length for the sub-domains MED, WCA, SAH, ARP, CAF, NEAF, and SEAF. The LALIA times are shown in bold.

https://doi.org/10.5194/egusphere-2026-1636
Preprint. Discussion started: 8 April 2026

the northern and southern Hemispheres. DJF is the wet season in the northern (MED, WCA) and southern (SEAF) subregions. No clear pattern of distribution of extremes can be identified in either season.

The wettest periods (Table 2) are (with only one exception: 15-years in SEAF) in the first centuries (500 BCE to 200 CE) of the simulation for all subregions. The same applies only to the subregions WCA, SAH, and ARP in JJA (Table A1), while the wettest JJA periods in MED and CAF occur in the second half of the first, and the wettest JJA periods in NEAF and SEAF occur in the second millennium. The MED experienced its wettest summers (JJA) of the entire simulation under the influence of the 536/540 volcanic eruptions. The wettest DJF seasons (Table A2) are in contrast to the annually resolved precipitations series, almost all (with only one exception: 25-years in SAH) in the Common Era.

The driest periods (Figure 2) are mostly found, except in WCA, in the second millennium CE. It was particularly dry in the 17th and 18th centuries. The 10-years after the 536 CE eruption constitute the driest of the simulation in SAH. The same accounts for the JJA driest periods (Table A1), while JJA is the rainy season in SAH. The ARP also shows the driest JJA periods under the influence of the 536/540 volcanic eruptions, where this is also the rainy season. Other than that, the driest JJA periods are mostly found in the second millennium. Apart from these cases, the driest DJF periods (Table A2) are distributed over the entire simulated period. The driest DJF 10-years period in NEAF (its dry season) occurs after the volcanic eruptions of 536/540 CE.

In summary, the period following the consecutive volcanic eruptions of 536 and 540 CE stands out particularly clearly in terms of extremes within the transient simulation, which spans 2350 years and covers a large domain with diverse climate zones. It represents the coldest period of the entire simulation across a wide area and, in some subregions, also the wettest or driest period, especially at the seasonal scale. The following subsections therefore focus primarily on the period after these eruptions. For the sake of simplicity, we will henceforth refer to the particularly distinctive 15-year period from 536 to 550 CE as LALIA, without intending to redefine the broader LALIA period as it is understood in the literature. The very long transient simulation presented so far provides an excellent basis for long-term observations of the paleoclimate. However, since the following subsections focus on a particularly extreme event, we want to reduce the probability that this extreme event arose randomly from the model's internal variability. For this reason, we will, from now on, include the second realization of our simulation in the analysis.

3.2 Regional Anomalies

To gain a more detailed insight into the climate following the successive volcanic eruptions in 536 and 540 CE, we now focus on a shorter period and compare the two seasons June, July, and August (JJA) and December, January, and February (DJF), assessing the extent to which they deviate from the long-term average of 1 to 1850 CE. Here, we take advantage of the fact that two realizations are available for the sixth century (Table 1). Figure 4 shows the percentage of grid cells in each subregion exceeding the threshold of $\pm\sigma$, $\pm 2\sigma$, and $\pm 3\sigma$ above or below the mean of the Common Era for each year from 536 to 560 CE for DJF, while Figure 5 shows the same analysis for JJA. The left columns represent temperature anomalies in the first and second realization, and the right columns show precipitation anomalies in both realizations. DJF represents the wet winter season in MED and WCA, the dry winter season in SAH and ARP, the dry season in NEAF and the northern part of CAF, and the wet season in SEAF and the southern part of CAF. JJA corresponds to the dry summer season in MED and WCA, the

https://doi.org/10.5194/egusphere-2026-1636
Preprint. Discussion started: 8 April 2026

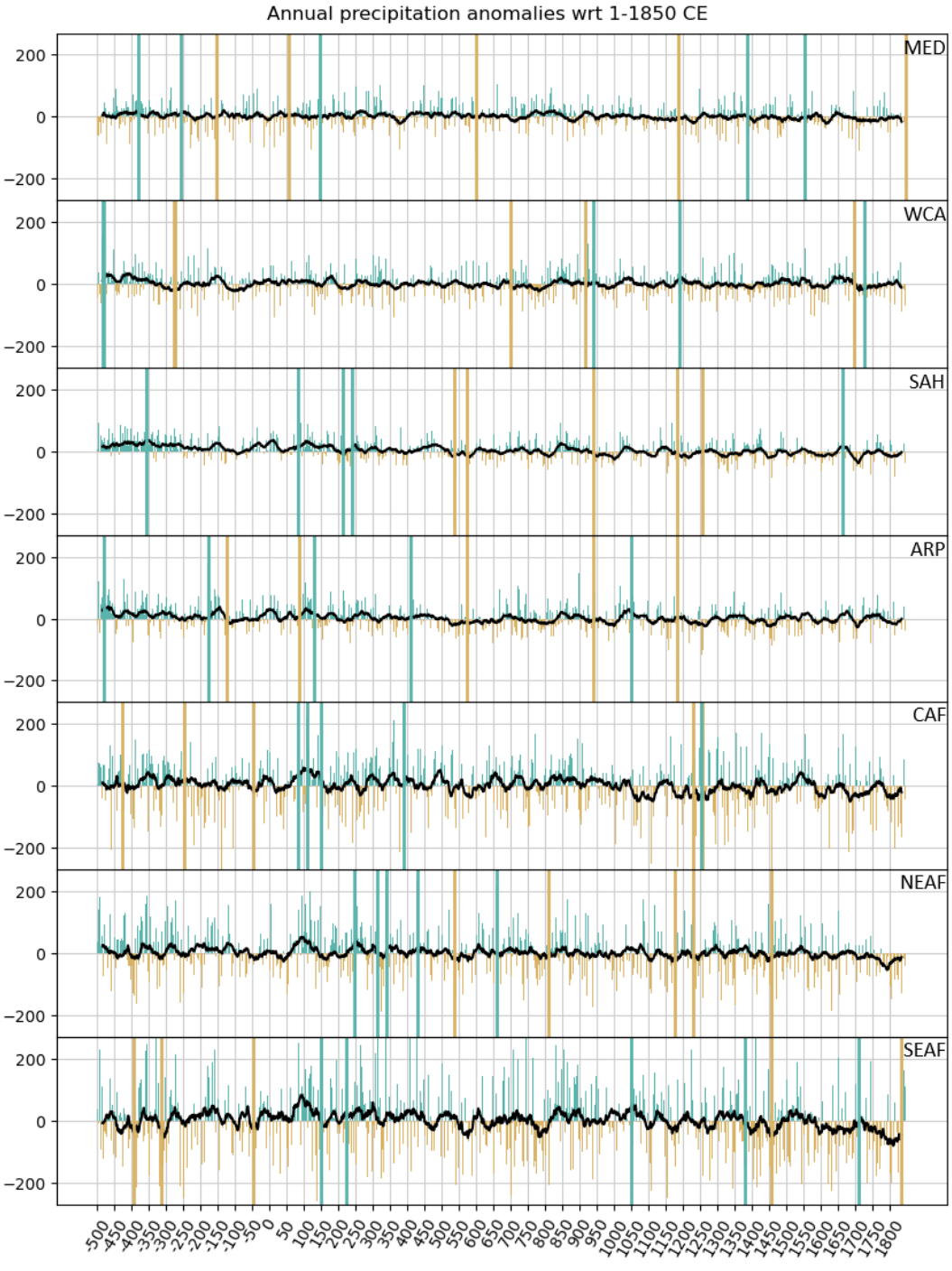

Figure 3. Precipitation anomalies for the MED, WCA, SAH, ARP, CAF, NEAF, and SEAF regions wrt 1-1850 CE for the entire simulated period from 500 BCE to 1850 CE with the 5 wettest and driest years highlighted as green and ochre bars, respectively, and the 30-year running mean in black.

https://doi.org/10.5194/egusphere-2026-1636
Preprint. Discussion started: 8 April 2026

wet summer season in SAH and ARP, the wet season in NEAF and northern CAF, and the dry season in SEAF and southern CAF. Generally, the lowest standard deviation for DJF temperature is found in SEAF, CAF, and NEAF, between 0.5 and 0.67 K, and the highest in WCA with 1.47 K. For precipitation, the lowest standard deviation is found in SAH and ARP, below 5 mm/month, and the highest in SEAF, above 30 mm/month, where a high standard deviation also reflects high precipitation amounts. In JJA, the standard deviations for temperature are relatively low in all subregions, ranging from 0.5 to 1 K, while the standard deviation for precipitation is highest in CAF, above 35 mm/month, and lowest in MED, WCA, and SEAF, around or below 10 mm/month.

In terms of DJF temperature, shown in Figure 4, both realizations agree in all subregions that between 540 and 550 CE most grid cells are cooler than the reference, although the anomalies are more pronounced in the first realization. The period of predominantly cooler conditions mostly begins in 537 and ends at the latest in 551. In most subregions, DJF in 541 shows the largest, or at least one of the largest, anomalies, and in some cases, large parts of the domain exceed the 3σ threshold, meaning that temperatures fall below 99.9% of DJF values in the respective subregion. After that, negative anomalies continue to dominate, but with decreasing intensity. The following years, between 550 and 560 CE, show either more positive temperature anomalies or no pronounced deviations. This does not support a sustained cold spell lasting more than one to two decades. The precipitation results are not as pronounced and do not show a consistent picture in both realizations. However, in the years after the eruptions, namely 537 and 541, precipitation is significantly lower in CAF and SEAF, meaning that the wet season is drier than normal, while precipitation in NEAF is almost constantly below the reference between 540 and 550, indicating that the dry seasons become even drier.

The JJA temperatures shown in Figure 5 are also cooler in the years after the eruptions. In the northern subregions MED, WCA, and parts of SAH and ARP, immediately after the first eruption in 536 CE, the negative anomalies are particularly strong, with large parts exceeding the 3σ interval. After the second eruption in 540 CE, which was tropical unlike the first eruption in the Northern Hemisphere, all subregions show profound negative anomalies. Again, MED and WCA show the largest cooling effect, where at least 50% of the MED area in the year 541 CE is colder than 99.9% of the summers. Very large effects are no longer visible after 544 CE in any of the subregions. Thus, JJA cooling is considerably more intense but shorter-lived than DJF cooling. Summer (JJA) precipitation in MED and WCA, which is naturally low, is clearly increased after the eruptions. Large parts of MED indicate more precipitation than 99.9% of the Common Era summers for up to 10 years after the first eruption. In contrast, SAH and ARP are drier in the years up to 545 CE, meaning that the dry season is amplified. CAF and NEAF also do not show any clear signal. In SEAF, it seems that the two to four years after the eruptions are slightly wetter during the dry season.

In summary, JJA experienced a short period of particularly strong cooling, whereas DJF remained significantly cooler over a longer interval across the entire domain. At the same time, summers in MED and WCA were wetter than average, while SAH, ARP, and NEAF tended to be drier after the volcanic eruptions. In SEAF, the dry seasons were slightly wetter than usual, while the rainy seasons were drier than normal. Due to the heterogeneous hydroclimatology of CAF, no clear conclusion can be drawn here.

https://doi.org/10.5194/egusphere-2026-1636
Preprint. Discussion started: 8 April 2026

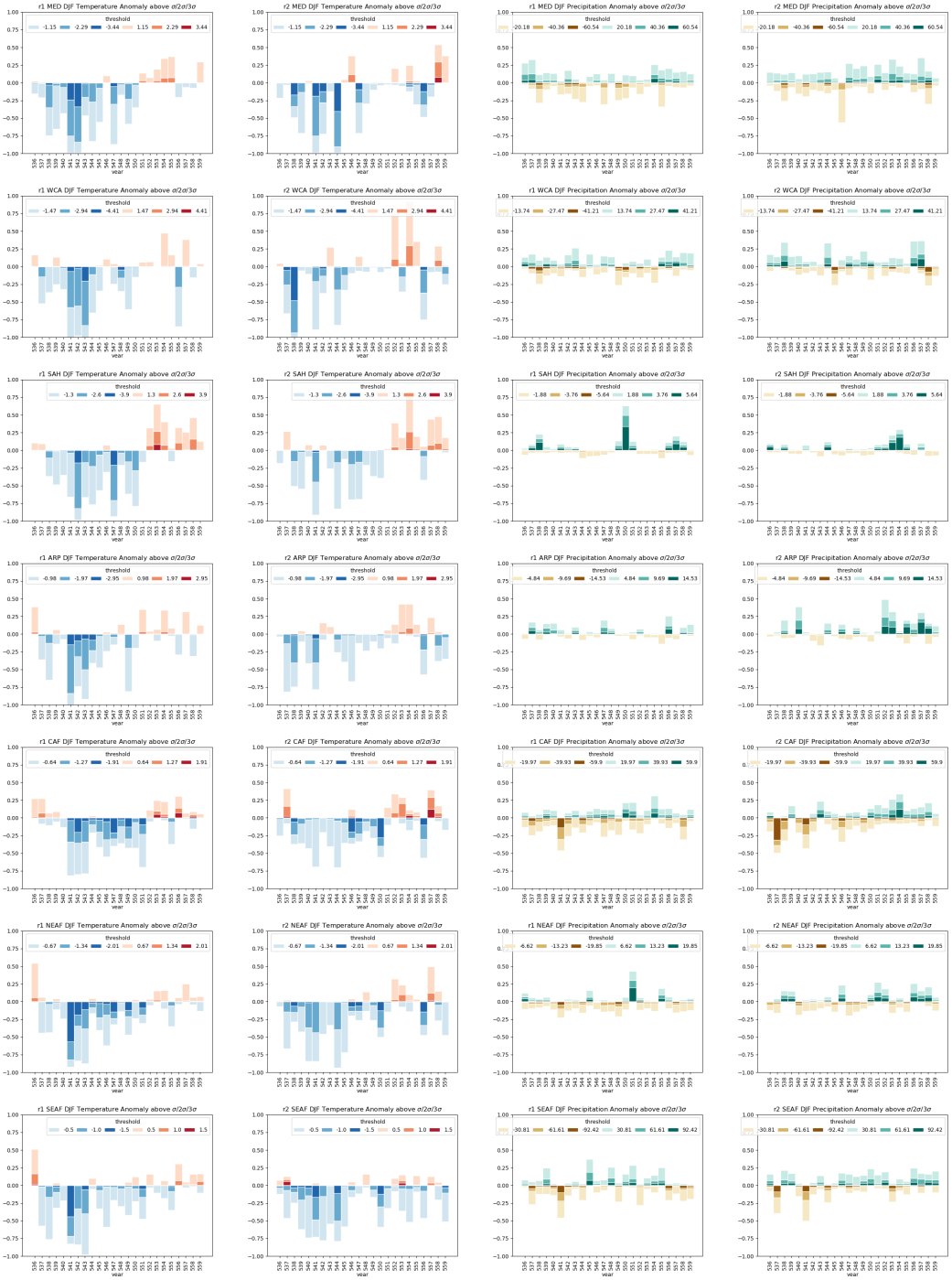

Figure 4. DJF Temperature and Precipitation anomalies in the subregions between 536 and 560 CE wrt to 1-1850 CE for the two realizations. Shown is the proportion of grid cells exceeding the threshold.

https://doi.org/10.5194/egusphere-2026-1636
Preprint. Discussion started: 8 April 2026

Figure 5. JJA Temperature and Precipitation anomalies in the subregions between 536 and 560 CE wrt to 1-1850 CE for the two realizations. Shown is the proportion of grid cells exceeding the threshold.

https://doi.org/10.5194/egusphere-2026-1636
Preprint. Discussion started: 8 April 2026

3.3 Annual Cycle

To bridge the gap between the annual variations and the high-resolution seasonal data considered so far, we now examine the annual cycle of temperature and precipitation in all subregions, which differ substantially (Figure 6). The MED and WCA regions show the lowest temperatures during boreal winter but reach high values during summer, while the colder months are characterized by moderate mid-latitude precipitation and the warm summer months by very low precipitation. SAH and ARP also show the typical Northern Hemisphere annual cycle, albeit with higher temperature levels. Precipitation amounts are very low except for the months of July, August, and September. The climate diagrams of CAF, NEAF, and SEAF follow different structures, with two temperature peaks, one between March and May and a second between September and October, which is clearly lower. Precipitation in CAF and SEAF is also bimodal, with a lower peak between March and May and a main maximum between September and December. In contrast, NEAF shows almost no precipitation during the months from December to February but large amounts between May and October. Overall the highest precipitation sums occur in CAF, with more than 200 mm/month in September and October, and still high values of more than 50 mm/month in the driest months, January and February. It should be noted that this is the average value for both the northern and southern hemispheres. The climate diagram may therefore vary significantly at specific locations within the subregion. SEAF and NEAF record the second-highest rainfalls, with at least a few months reaching 100 mm/month. The driest regions are SAH and ARP, with precipitation below 10 mm/month in the majority of months and only a few months during boreal summer reaching values above 50 mm/month. The lowest temperatures occur in WCA, where the highest elevations are, with values below 275 K, followed by MED, with minimum values down to 280 K. The highest minimum temperature occurs in CAF, remaining above 295 K. The highest values, with up to 305 K, occur in SAH and ARP, while the lowest maximum value is found in SEAF, with around 296 K. In summary, CAF, NEAF, and SEAF have the smallest annual temperature amplitude but the highest variation in precipitation, which is also associated with high variability within the subdomains. SAH and ARP have a higher temperature amplitude but very low annual precipitation. MED and especially WCA show the largest temperature variation with medium amounts of precipitation, although fluctuations within the subdomains can also be large here.

The mean for the years 536 to 550 CE, referred to as LALIA in both realizations, as well as the mean for the Common Era, agree well in terms of their general structure. The differences between LALIA and the Common Era means are shown to the right of each climate diagram in Figure 6. The differences between the regions are very pronounced, and differences between the realizations are also apparent, but they do not contradict each other. In MED and WCA during the LALIA period, temperatures are between 0.5 and 1.5 K cooler in all months. Precipitation differences are small and not always clear, especially in WCA, which has a high hydroclimatological heterogeneity. For MED, there is a tendency towards higher precipitation of up to 5 mm/month between April and November, which can be up to twice the reference precipitation amount. In SAH, temperatures are also up to 1.5 K cooler except for the rainy season between July and September. Here, temperature differences are small, but precipitation amounts clearly decrease by up to 12 mm/month, which is about 20% of the total amount. ARP shows a similar behavior, but the temperature decrease is up to 1 K smaller, whereas the decrease in precipitation during the rainy season is up to 15 mm/month, which is 25% of the total, while in October precipitation increases by more than 30%. In CAF

https://doi.org/10.5194/egusphere-2026-1636
Preprint. Discussion started: 8 April 2026

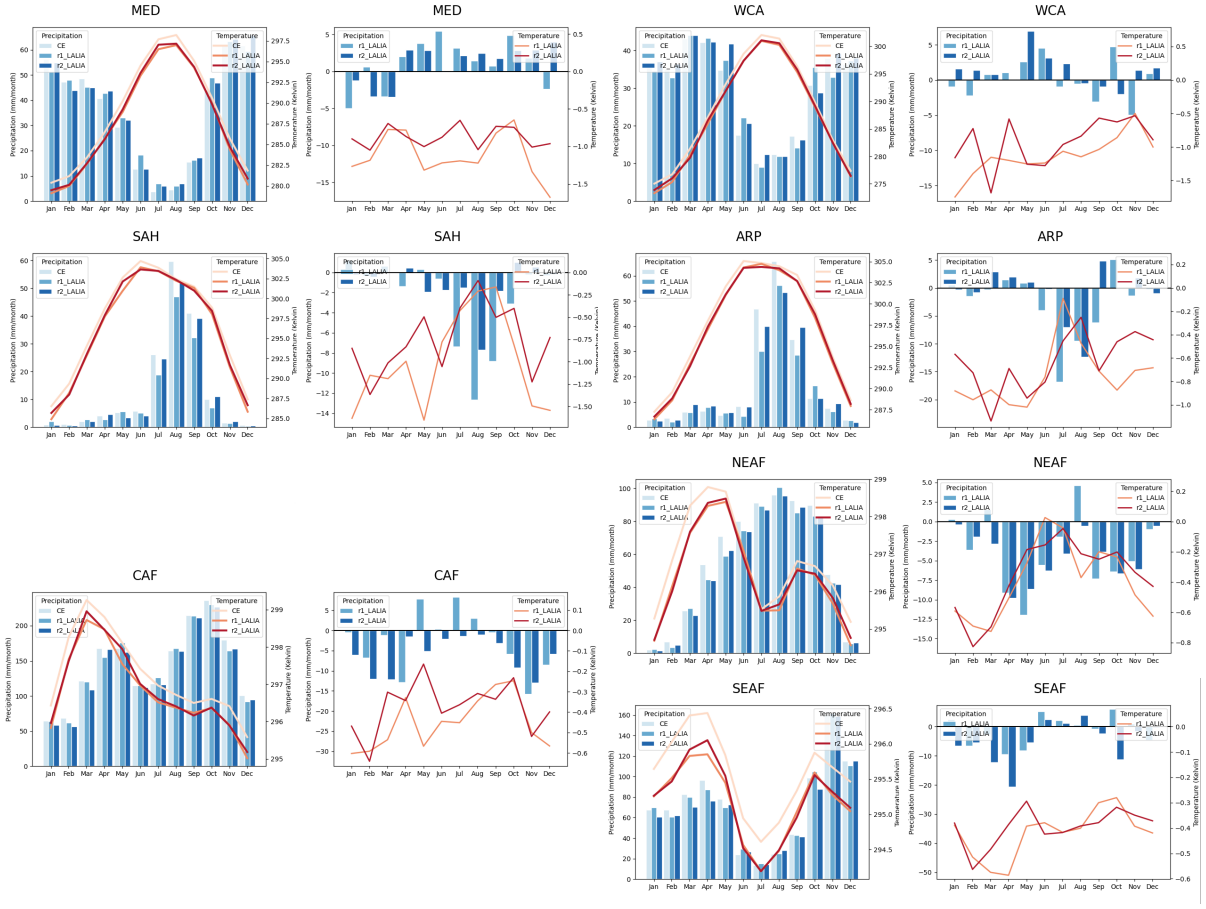

Figure 6. Climate Diagrams for each of the subregions for 1-1850 CE and the LALIA (536-550 CE) period on the left and the anomalies for LALIA with both realizations wrt 1-1850 CE on the right.

and SEAF, the cooling varies between 0.2 and 0.6 K, while in NEAF the cooling is most pronounced between January and March, with up to 0.8 K, and remains below 0.2 K between May and October. The precipitation anomalies also vary strongly between the regions, and certainly also within the subregions. In CAF, there is less precipitation between October and April, with up to 15 mm/month less. In NEAF, precipitation decreases between April and July and from September to November by up to 10 mm/month, with the largest effects occurring in April and November, when total precipitation is only moderate, but the anomaly is high. In SEAF, the precipitation decrease is small and only noticeable between March and May.

Overall, these results are consistent with findings from previous studies. MED and WCA remain considerably colder than average throughout the LALIA period, accompanied by increased precipitation during the usually dry summer months. SAH and ARP are also colder than the long-term average, particularly during the dry seasons, while the rainy season is weakened during LALIA. In CAF, NEAF, and SEAF, cooling is likewise more pronounced during the dry months, and the rainy seasons in all three subregions are drier during LALIA.

https://doi.org/10.5194/egusphere-2026-1636
Preprint. Discussion started: 8 April 2026

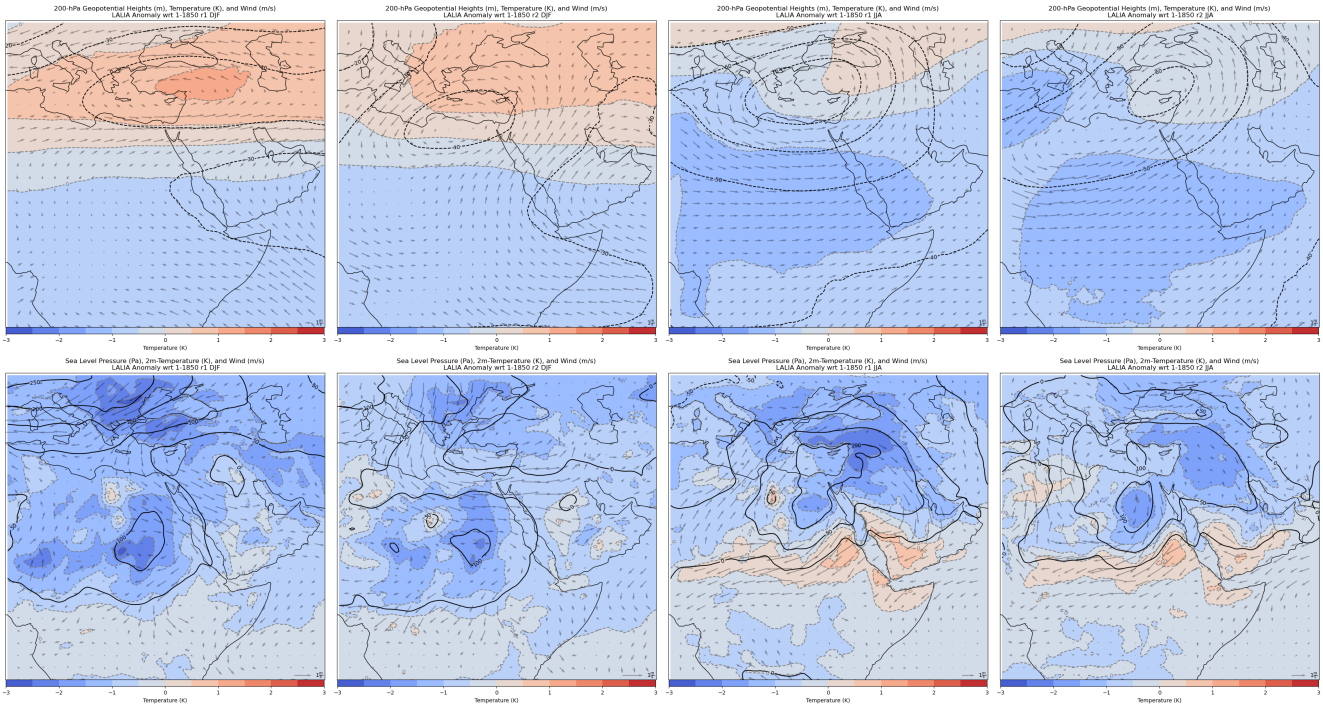

Figure 7. Geopotential height (top row) and sea level pressure (SLP, bottom row) as contour together with temperature (colors) and wind (arrows) in 200 hPa (top row) and at the surface (bottom row, 2m temperature and 850 hPa wind) as anomaly between 536 and 550 CE wrt 1-1850 CE for DJF (two left columns) and JJA (two right columns) and both realizations.

3.4 Atmospheric Circulation

In order to better contextualize the previously presented findings on climate anomalies in the subregions during LALIA, we now examine the large-scale atmospheric circulation. For this purpose, we compare pressure conditions, including geopotential height and sea level pressure, temperatures, and flow patterns represented by wind fields at the upper and lower levels of the troposphere. We assume an average tropopause height of 200 hPa as the upper level. For the lower atmosphere, we consider pressure reduced to sea level (SLP), 2m temperature, and wind at 850 hPa to reduce the dependence on surface roughness. Figure 7 compares, for both realizations, the atmospheric circulation during the period 536 to 550 CE with the entire Common Era as a reference for JJA and DJF. In addition, temperature and wind anomalies at selected levels are shown relative to the Common Era mean.

For DJF, more cyclonic structures are evident over the eastern Mediterranean, the Middle East, and the Arabian Peninsula, accompanied by enhanced northerly to northeasterly winds over the Balkans. Westerly winds prevail over the northeastern Sahara and the Arabian Peninsula. As a meteorological consequence of the intensified northerly flow, the strongest negative temperature anomalies occur over the Balkans, Anatolia, and the eastern Sahara. This pattern is associated with increased cyclonic activity at 200 hPa over the same region, while the more cyclonic flow at about 12 km height transports warmer air

https://doi.org/10.5194/egusphere-2026-1636
Preprint. Discussion started: 8 April 2026

masses from the tropics toward the midlatitudes.

In JJA, anticyclonic winds and higher surface pressure are centered over the core of the domain and extend across nearly the entire Northern Hemisphere part of the study area. Pronounced negative temperature anomalies occur over Anatolia, the Levant, and the lower Nile region, possibly linked to weaker Etesian winds. Conversely, positive temperature anomalies appear between 10°N and 20°N, coinciding with the position of the ITCZ during boreal summer. Areas around the southern Red Sea, which are strongly influenced by the Indian summer monsoon during these months, show a distinct warming. At 200 hPa, geopotential heights are reduced throughout the domain, indicating stronger cyclonic circulation. Despite the surface warming in some regions, temperatures at approximately 12 km height are cooler than the Common Era mean across the entire domain.

4 Conclusions

This study analyzes the transient regional climate of the last 2500 years, with particular emphasis on the climatic response to the closely spaced volcanic eruptions of 536 and 540 CE across a set of contrasting subregions. The domain covers the eastern Mediterranean, the Middle East, the Sahara, the Arabian Peninsula, and large parts of Central, Northeast, and Southeast Africa, thereby encompassing Mediterranean, temperate, desert, and tropical climatic regimes across both the Northern Hemisphere and parts of the Southern Hemisphere. The simulations span the period from 500 BCE to 1850 CE and include two realizations with identical external forcing but different initial conditions for the sixth century. This small ensemble allows us to assess the robustness of the simulated response against internal variability. Across the full transient simulation period, both temperature and precipitation show pronounced variability, but the strongest coherence among subregions is associated with major volcanic eruptions. This is particularly evident for the mid-sixth-century eruption cluster, which therefore provides an especially valuable case for detailed analysis.

Both realizations show a clear and spatially extensive cooling in the years following the eruptions. The strongest temperature anomalies occur within the first one to five post-eruption years, while weaker but still discernible cooling persists for up to about 15 years. At the same time, the response is not spatially uniform and differs substantially by season and climatic regime. Cooling is generally more pronounced during dry seasons than during wet seasons, while precipitation anomalies vary strongly by region. In the eastern Mediterranean and Western Central Asia, summers become markedly wetter despite being climatologically dry, with Mediterranean summer precipitation locally reaching up to about twice the long-term mean. In contrast, the Sahara and the Arabian Peninsula experience substantially reduced precipitation during their boreal summer rainy season, with decreases of up to about 25%. Central and Northeast Africa also show drier conditions during the rainy seasons, especially during the transitional months. These results demonstrate that the climatic response to the 536 and 540 CE eruptions cannot be understood in terms of cooling alone, but must be interpreted through the combined lens of temperature, hydroclimate, and circulation changes.

The northernmost subregions, MED and WCA, exhibit the strongest and most persistent temperature response, with negative anomalies frequently exceeding the 2σ interval. MED also shows a clear increase in precipitation, especially during the normally dry summer months, indicating that the eastern Mediterranean experienced not only colder years overall but also

https://doi.org/10.5194/egusphere-2026-1636
Preprint. Discussion started: 8 April 2026

distinctly colder and wetter summers. WCA shows a similar but weaker hydroclimatic tendency, likely reflecting its stronger internal spatial heterogeneity and complex orographic structure. The desert-dominated regions SAH and ARP also undergo several years of severe cooling, especially during the dry season in boreal winter. In contrast, their rainy season becomes markedly drier, while only limited cooling is evident during those months. In tropical Africa, the response is likewise seasonally differentiated, and can fluctuate significantly both between and within subregions. CAF experiences colder and drier conditions, particularly during the dry season, while wet season precipitation is also reduced. NEAF is considerably cooler during the dry season and somewhat drier during the wet season. SEAF is cooler throughout the year, drier during the wet season, and slightly wetter during the dry season. Taken together, these results highlight a robust but regionally contrasting climatic response across the study domain. It should not be neglected that the subregions themselves are geographically and climatically heterogeneous, some more so than others. Although we derive these results solely from a modeled version of reality, we can, based on the simulations run twice with varying initial conditions and using the most up-to-date external forcings, fairly confidently confirm the extremely harsh climatic conditions in the 540s within our study area.

The simulated circulation anomalies provide a physically consistent explanation for these patterns. The results point to a possible weakening and reorganization of large-scale circulation systems, including suggested shifts in the ITCZ-related hydroclimate regime, and likely, a weakening of the Indian monsoon influence. Reduced incoming solar radiation after the eruptions cools the surface and thus weakens land-sea thermal contrasts. In summer, this likely reduces the influence of the Etesians over the Mediterranean and favors a greater influence of maritime air masses, thereby increasing humidity and precipitation in MED. In contrast, regions more directly tied to the seasonal migration of the ITCZ and monsoonal flow seem to receive less moisture, contributing to drier rainy seasons in SAH, ARP, CAF, NEAF, and parts of SEAF. More generally, diminished radiative input can reduce the energy available for evaporation and moisture supply, reinforcing possible precipitation deficits in several subregions. The results therefore suggest that the climatic impact of the volcanic eruptions resulted not only from direct radiative cooling, but possibly also from substantial circulation-driven and hydroclimatic adjustments.

A central result of this study is that the post-eruption cooling in our domain, although pronounced, is temporally limited. In most regions, the strongest effects occur between 536 and about 545 CE, and in nearly all cases, they fade by around 550 CE. The simulations therefore do not support a continuously sustained cold period lasting several decades in this region. Instead, they indicate a relatively sharp and intense climatic perturbation followed by a return toward pre-eruption conditions, until later volcanic events imposed new disturbances. In this respect, our results point to a shorter duration of severe cooling than has sometimes been inferred from studies centered on Central Europe or the broader Northern Hemisphere, while remaining consistent with modeling work that emphasizes spatial heterogeneity and regionally variable persistence of volcanic impacts.

More broadly, this study demonstrates the value of transient regional climate simulations for reconstructing and interpreting past climate variability in historically important but climatically diverse regions. The simulations provide spatially explicit and seasonally resolved climate information that is difficult to obtain from proxy records alone and therefore offer an important basis for comparison with natural archives, documentary evidence, and historical observations. They also provide a physically coherent framework for future interdisciplinary work linking climate anomalies to impacts on water resources, agriculture, food systems, mobility, health, and political or economic stability during Late Antiquity. In this way, the present simulations

https://doi.org/10.5194/egusphere-2026-1636
Preprint. Discussion started: 8 April 2026

help move beyond generalized narratives of volcanic cooling toward a more regionally differentiated understanding of how abrupt climatic forcing interacted with environmental and societal conditions. Such work is not only relevant for interpreting the past, but can also inform broader discussions of vulnerability, resilience, and adaptation under conditions of climatic stress today and in the future (Comfort et al., 2010; Moreland, 2018; Peregrine, 2020).

Code and data availability. The COSMO-CLM model is available for all members of the CLM-Community via their website www.clm-community.eu. It is free of charge for all research applications. Either the user needs to be a member of the CLM-Community or the respective institute needs to hold an institutional license. The changes published by Hartmann et al. (2025) can be made accessible for CLM-COmmunity members at the Zenodo repository (10.5281/zenodo.14288621).
The simulation results are archived at DKRZ and are available upon request to the authors. The monthly, seasonal, and annual temperature and precipitation data used for this analysis are uploaded to the Zenodo repository (10.5281/zenodo.18926603). Plot scripts are also available at a Zenodo repository (10.5281/zenodo.18924322).

Author contributions. EH performed the RCM simulations. SW performed the ESM simulations. EX and JL supervised the project. EH conducted the formal analysis with the support of EX and SW. EX, JL, SW, and EH contributed to the conceptualization of the manuscript. EH prepared the manuscript. All authors contributed to the discussion of the results and editing of the manuscript.

Competing interests. At least one of the (co-)authors is a member of the editorial board of Climate of the Past. Other than that, the authors declare that they have no conflict of interest.

Acknowledgements. This work used resources of the Deutsches Klimarechenzentrum (DKRZ) granted by its Scientific Steering Committee (WLA) under project number bb1201. EX acknowledges support from the ERC Synergy project EUROpest (grant number 101166700).

Appendix A: JJA and DJF timeseries and extreme periods from 500 BCE to 1850 CE

https://doi.org/10.5194/egusphere-2026-1636
Preprint. Discussion started: 8 April 2026

		10-years	15-years	20-years	25-years	30-years
cold	MED	**536 - 546**	**535 - 550**	**536 - 556**	**535 - 560**	**536 - 566**
	WCA	**535 - 545**	**535 - 550**	**535 - 555**	**529 - 554**	**530 - 560**
	SAH	**539 - 549**	-218 - -203	-231 - -211	-228 - -203	-232 - -202
	ARP	-395 - -385	-397 - -382	-401 - -381	-407 - -382	1257 - 1287
	CAF	**537 - 547**	**536 - 551**	**539 - 559**	**536 - 561**	**530 - 560**
	NEAF	-427 - -417	672 - 687	681 - 701	674 - 699	673 - 703
	SEAF	-48 - -38	-52 - -37	-48 - -28	-54 - -29	1258 - 1288
warm	MED	-1 - 9	-6 - 9	-3 - 17	-6 - 19	-460 - -430
	WCA	-343 - -333	-345 - -330	-341 - -321	-347 - -322	-344 - -314
	SAH	1628 - 1638	1625 - 1640	1618 - 1638	1613 - 1638	1609 - 1639
	ARP	1744 - 1754	1625 - 1640	1488 - 1508	1727 - 1752	1728 - 1758
	CAF	1100 - 1110	1748 - 1763	1046 - 1066	1079 - 1104	1077 - 1107
	NEAF	1744 - 1754	804 - 819	800 - 820	1612 - 1637	1608 - 1638
	SEAF	1549 - 1559	1422 - 1437	1423 - 1443	1533 - 1558	1422 - 1452
wet	MED	**536 - 546**	**534 - 549**	**530 - 550**	**520 - 545**	**536 - 566**
	WCA	-156 - -146	-162 - -147	-166 - -146	-167 - -142	-168 - -138
	SAH	0 - 10	1 - 16	2 - 22	-1 - 24	-5 - 25
	ARP	-3 - 7	-6 - 9	98 - 118	89 - 114	89 - 119
	CAF	886 - 896	717 - 732	717 - 737	642 - 667	643 - 673
	NEAF	1425 - 1435	55 - 70	1423 - 1443	1416 - 1441	1413 - 1443
	SEAF	1371 - 1381	1427 - 1442	1423 - 1443	1425 - 1450	1423 - 1453
dry	MED	1145 - 1155	1037 - 1052	1826 - 1846	1820 - 1845	1537 - 1567
	WCA	1382 - 1392	577 - 592	1382 - 1402	1338 - 1363	1331 - 1361
	SAH	**536 - 546**	1694 - 1709	1700 - 1720	1694 - 1719	1694 - 1724
	ARP	**536 - 546**	**535 - 550**	**527 - 547**	**520 - 545**	**515 - 545**
	CAF	1381 - 1391	1380 - 1395	248 - 268	-211 - -186	248 - 278
	NEAF	1051 - 1061	1044 - 1059	1787 - 1807	1044 - 1069	1047 - 1077
	SEAF	1800 - 1810	1794 - 1809	1790 - 1810	1228 - 1253	1226 - 1256

Table A1. JJA coldest, warmest, wettest, and driest periods of 10, 15, 20, 25, and 30 years length for the sub-domains MED, WCA, SAH, ARP, CAF, NEAF, and SEAF. The LALIA times are shown in bold.

https://doi.org/10.5194/egusphere-2026-1636
Preprint. Discussion started: 8 April 2026

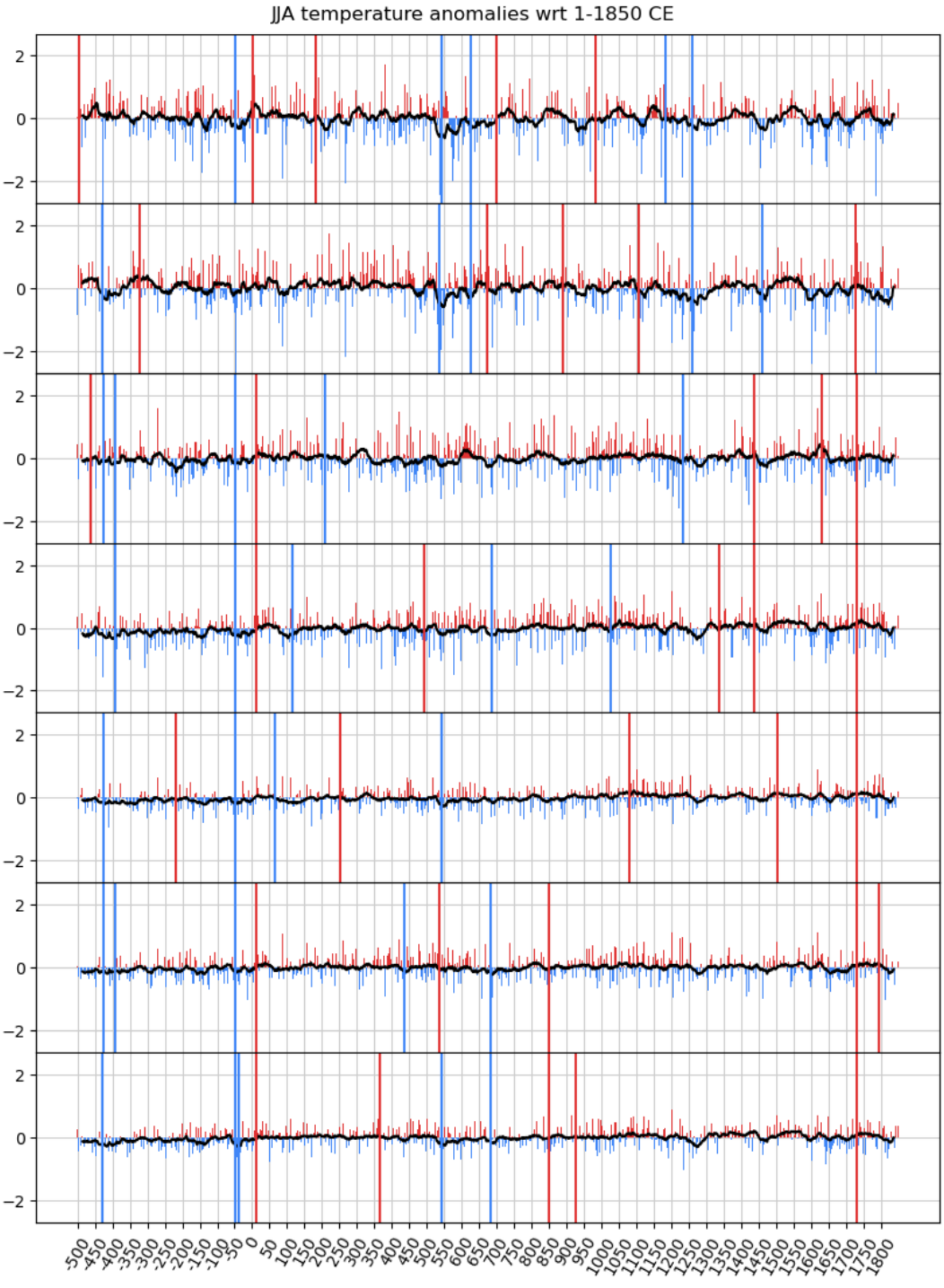

Figure A1. JJA temperature anomalies for the MED, WCA, SAH, ARP, CAF, NEAF, and SEAF regions wrt 1-1850 CE for the entire simulated period from 500 BCE to 1850 CE with the 5 warmest and coldest years highlighted as red and blue bars, respectively, and the 30-year running mean in black.

https://doi.org/10.5194/egusphere-2026-1636
Preprint. Discussion started: 8 April 2026

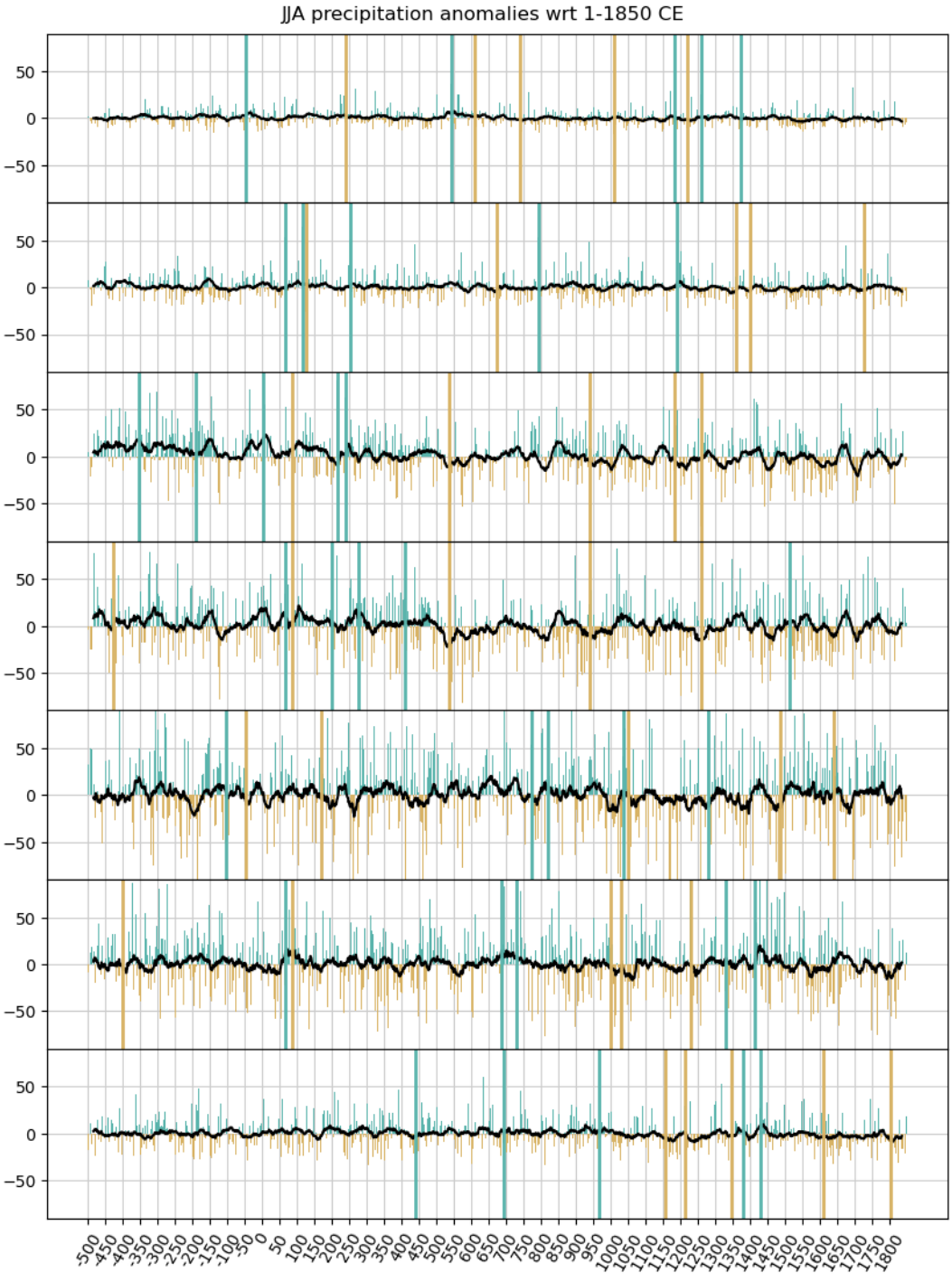

Figure A2. As Figure 2 but for JJA Precipitation anomalies with the 5 wettest and driest years highlighted as green and ochre bars, respectively, and the 30-year running mean in black.

https://doi.org/10.5194/egusphere-2026-1636
Preprint. Discussion started: 8 April 2026

		10-years	15-years	20-years	25-years	30-years
cold	MED	**536 - 546**	**535 - 550**	**533 - 553**	**525 - 550**	**529 - 559**
	WCA	**536 - 546**	**536 - 551**	**533 - 553**	**525 - 550**	**521 - 551**
	SAH	**539 - 549**	**536 - 551**	**532 - 552**	**525 - 550**	**521 - 551**
	ARP	**536 - 546**	1820 - 1835	1816 - 1836	1810 - 1835	1807 - 1837
	CAF	-48 - -38	**536 - 551**	**532 - 552**	-494 - -469	-494 - -464
	NEAF	-48 - -38	**536 - 551**	1810 - 1830	1811 - 1836	1810 - 1840
	SEAF	-48 - -38	**536 - 551**	1258 - 1278	1257 - 1282	1258 - 1288
warm	MED	376 - 386	353 - 368	349 - 369	355 - 380	356 - 386
	WCA	964 - 974	609 - 624	-287 - -267	-292 - -267	-295 - -265
	SAH	609 - 619	1655 - 1670	1651 - 1671	1650 - 1675	1652 - 1682
	ARP	273 - 283	269 - 284	371 - 391	1666 - 1691	1662 - 1692
	CAF	317 - 327	1158 - 1172	241 - 261	238 - 263	1142 - 1172
	NEAF	1627 - 1637	1666 - 1681	1535 - 1555	1533 - 1558	1529 - 1559
	SEAF	1627 - 1637	1421 - 1436	359 - 379	359 - 384	1353 - 1383
wet	MED	970 - 980	964 - 979	962 - 982	961 - 986	256 - 286
	WCA	526 - 536	521 - 536	517 - 537	1671 - 1696	1667 - 1697
	SAH	108 - 118	106 - 121	104 - 124	-393 - -368	105 - 135
	ARP	427 - 437	622 - 637	270 - 290	1670 - 1695	1645 - 1675
	CAF	92 - 102	86 - 101	90 - 110	84 - 109	86 - 116
	NEAF	1686 - 1696	1689 - 1704	1521 - 1541	1687 - 1712	1691 - 1721
	SEAF	666 - 676	94 - 109	93 - 113	1221 - 1246	80 - 110
dry	MED	1231 - 1241	136 - 151	1325 - 1345	132 - 157	121 - 151
	WCA	358 - 368	1264 - 1279	1260 - 1280	1254 - 1279	1250 - 1280
	SAH	918 - 928	917 - 932	918 - 938	919 - 944	916 - 946
	ARP	-303 - -293	637 - 652	639 - 659	-277 - -252	638 - 668
	CAF	1640 - 1650	1230 - 1245	1099 - 1119	1080 - 1105	1062 - 1092
	NEAF	**540 - 550**	1257 - 1272	-115 - -95	749 - 774	747 - 777
	SEAF	1809 - 1819	1806 - 1821	1458 - 1478	1796 - 1821	1807 - 1837

Table A2. DJF coldest, warmest, wettest, and driest periods of 10, 15, 20, 25, and 30 years length for the sub-domains MED, WCA, SAH, ARP, CAF, NEAF, and SEAF. The LALIA times are shown in bold.

https://doi.org/10.5194/egusphere-2026-1636
Preprint. Discussion started: 8 April 2026

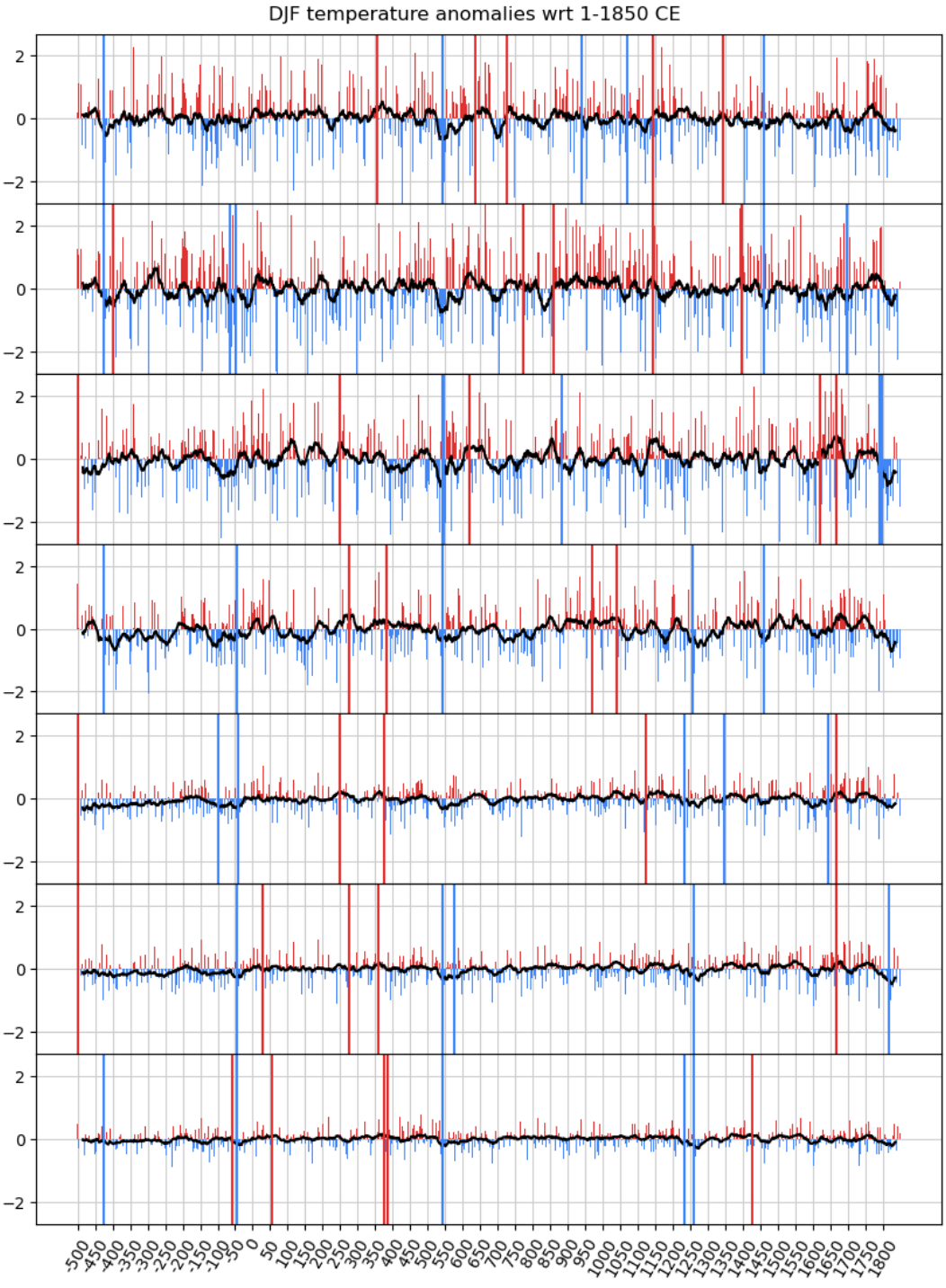

Figure A3. DJF temperature anomalies for the MED, WCA, SAH, ARP, CAF, NEAF and SEAF regions wrt 1-1850 CE for the entire simulated period from 500 BCE to 1850 CE with the 5 warmest and coldest years highlighted as red and blue bars, respectively, and the 30-year running mean in black.

https://doi.org/10.5194/egusphere-2026-1636
Preprint. Discussion started: 8 April 2026

References

2k Consortium', P.: Continental-scale temperature variability during the past two millennia, Nature Geoscience, 6, 339–346, https://doi.org/https://doi.org/10.1038/ngeo1797, 2013.

Attada, R., Dasari, H. P., Parekh, A., Chowdary, J. S., Langodan, S., Knio, O., and Hoteit, I.: The role of the Indian summer monsoon variability on Arabian Peninsula summer climate, Climate Dynamics, 52, 3389–3404, https://doi.org/10.1007/s00382-018-4333-x, 2019.

Baldauf, M., Seifert, A., Förstner, J., Majewski, D., Raschendorfer, M., and Reinhardt, T.: Operational Convective-Scale Numerical Weather Prediction with the COSMO Model: Description and Sensitivities, Monthly Weather Review, 139, 3887 – 3905, https://doi.org/10.1175/MWR-D-10-05013.1, 2011.

Beck, H. E., McVicar, T. R., Vergopolan, N., Berg, A., Lutsko, N. J., Dufour, A., Zeng, Z., Jiang, X., van Dijk, A. I., and Miralles, D. G.: High-resolution (1 km) Köppen-Geiger maps for 1901–2099 based on constrained CMIP6 projections, Scientific data, 10, 724, https://doi.org/10.1038/s41597-023-02549-6, 2023.

Berger, A.: Long-Term Variations of Daily Insolation and Quaternary Climatic Changes, Journal of the Atmospheric Sciences, 35, 2362–2367, https://doi.org/10.1175/1520-0469(1978)035<2362:LTVODI>2.0.CO;2, 1978.

Bradley, R. S.: Paleoclimatology: Reconstructing Climates of the Quaternary (3rd edition), Elsevier, ISBN 9780123869135, 2014.

Brázdil, R., Pfister, C., Wanner, H., Storch, H. V., and Luterbacher, J.: Historical climatology in Europe–the state of the art, Climatic change, 70, 363–430, https://doi.org/10.1007/s10584-005-5924-1, 2005.

Bucchignani, E., Cattaneo, L., Panitz, H.-J., and Mercogliano, P.: Sensitivity analysis with the regional climate model COSMO-CLM over the CORDEX-MENA domain, Meteorology and Atmospheric Physics, 128, 73–95, https://doi.org/10.1007/s00703-015-0403-3, 2016.

Büntgen, U., Myglan, V. S., Ljungqvist, F. C., McCormick, M., Di Cosmo, N., Sigl, M., Jungclaus, J., Wagner, S., Krusic, P. J., Esper, J., Kaplan, J. O., de Vaan, M. A. C., Luterbacher, J., Wacker, L., Tegel, W., and Kirdyanov, A. V.: Cooling and societal change during the Late Antique Little Ice Age from 536 to around 660 AD, Nature Geoscience, 9, 231–236, https://doi.org/10.1038/ngeo2652, 2016.

Burgdorf, A.-M.: A global inventory of quantitative documentary evidence related to climate since the 15th century, Climate of the Past, 18, 1407–1428, https://doi.org/10.5194/cp-18-1407-2022, 2022.

Büntgen, U., Arseneault, D., Étienne Boucher, Churakova (Sidorova), O. V., Gennaretti, F., Crivellaro, A., Hughes, M. K., Kirdyanov, A. V., Klippel, L., Krusic, P. J., Linderholm, H. W., Ljungqvist, F. C., Ludescher, J., McCormick, M., Myglan, V. S., Nicolussi, K., Piermattei, A., Oppenheimer, C., Reinig, F., Sigl, M., Vaganov, E. A., and Esper, J.: Prominent role of volcanism in Common Era climate variability and human history, Dendrochronologia, 64, 125 757, https://doi.org/https://doi.org/10.1016/j.dendro.2020.125757, 2020.

Camberlin, P.: Rainfall Anomalies in the Source Region of the Nile and Their Connection with the Indian Summer Monsoon, Journal of Climate, 10, 1380 – 1392, https://doi.org/10.1175/1520-0442(1997)010<1380:RAITSR>2.0.CO;2, 1997.

Christiansen, B. and Ljungqvist, F. C.: Challenges and perspectives for large-scale temperature reconstructions of the past two millennia, Reviews of Geophysics, 55, 40–96, https://doi.org/https://doi.org/10.1002/2016RG000521, 2017.

Comfort, L. K., Boin, A., and Demchak, C. C.: Designing resilience: Preparing for extreme events, University of Pittsburgh Press, https://doi.org/10.2307/j.ctt5hjq0c, 2010.

Conedera, M., Tinner, W., Neff, C., Meurer, M., Dickens, A. F., and Krebs, P.: Reconstructing past fire regimes: methods, applications, and relevance to fire management and conservation, Quaternary Science Reviews, 28, 555 – 576, https://doi.org/https://doi.org/10.1016/j.quascirev.2008.11.005, 2009.

https://doi.org/10.5194/egusphere-2026-1636
Preprint. Discussion started: 8 April 2026

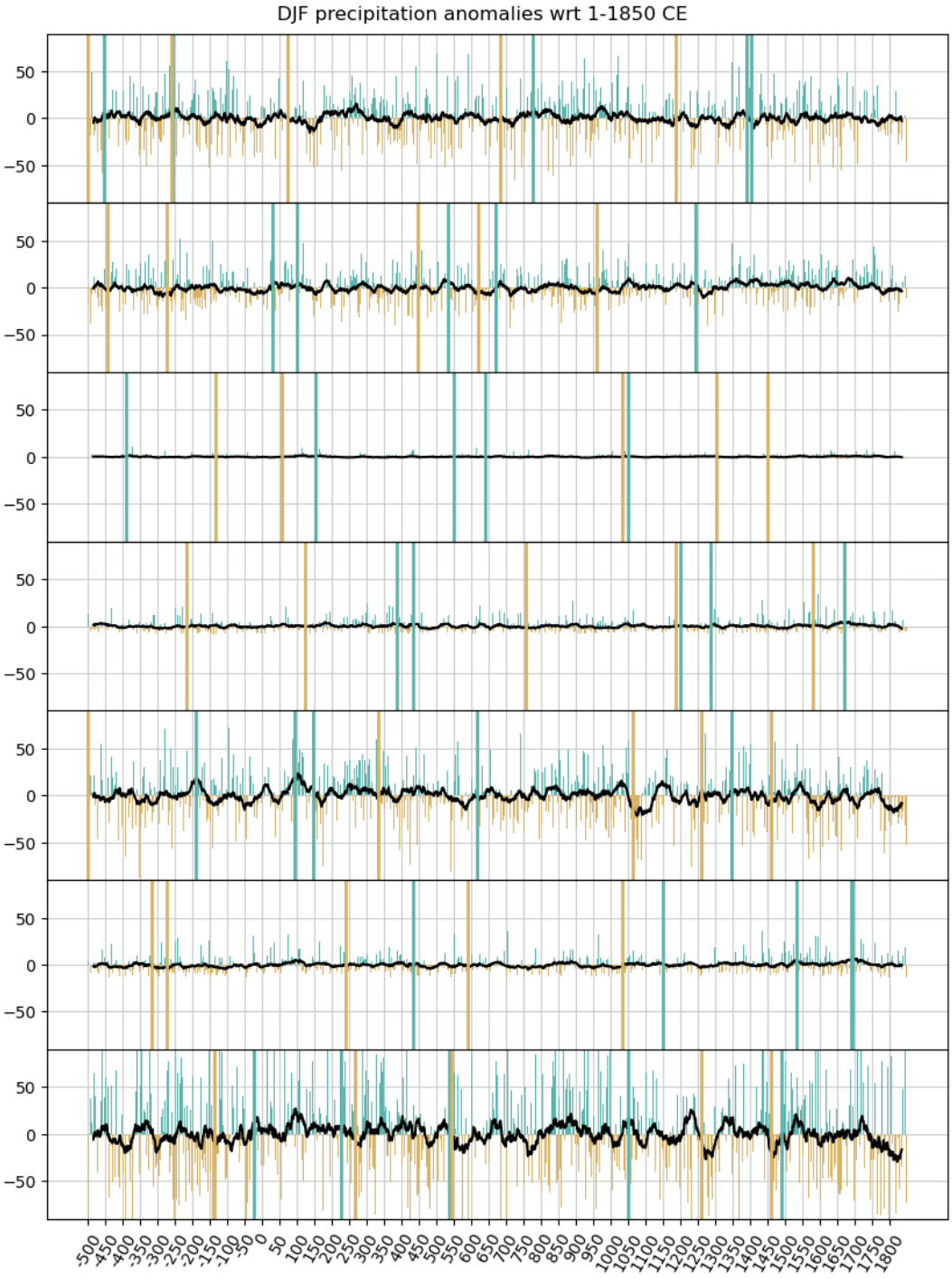

Figure A4. As Figure 2, but for DJF Precipitation anomalies with the 5 wettest and driest years highlighted as green and ochre bars, respectively, and the 30-year running mean in black.

https://doi.org/10.5194/egusphere-2026-1636
Preprint. Discussion started: 8 April 2026

Conroy, J. L., Cobb, K. M., Lynch-Stieglitz, J., and Polissar, P. J.: Constraints on the salinity–oxygen isotope relationship in the central tropical Pacific Ocean, Marine Chemistry, 161, 26 – 33, https://doi.org/https://doi.org/10.1016/j.marchem.2014.02.001, 2014.

Cook, E. R., Seager, R., Kushnir, Y., Briffa, K. R., Büntgen, U., Frank, D., Krusic, P. J., Tegel, W., van der Schrier, G., Andreu-Hayles, L., Baillie, M., Baittinger, C., Bleicher, N., Bonde, N., Brown, D., Carrer, M., Cooper, R., Čufar, K., Dittmar, C., Esper, J., Griggs, C., Gunnarson, B., Günther, B., Gutierrez, E., Haneca, K., Helama, S., Herzig, F., Heussner, K.-U., Hofmann, J., Janda, P., Kontic, R., Köse, N., Kyncl, T., Levanič, T., Linderholm, H., Manning, S., Melvin, T. M., Miles, D., Neuwirth, B., Nicolussi, K., Nola, P., Panayotov, M., Popa, I., Rothe, A., Seftigen, K., Seim, A., Svarva, H., Svoboda, M., Thun, T., Timonen, M., Touchan, R., Trotsiuk, V., Trouet, V., Walder, F., Ważny, T., Wilson, R., and Zang, C.: Old World megadroughts and pluvials during the Common Era, Science Advances, 1, e1500 561, https://doi.org/10.1126/sciadv.1500561, 2015.

Crowley, T. J. and North, G. R.: Abrupt Climate Change and Extinction Events in Earth History, Science, 240, 996–1002, https://doi.org/10.1126/science.240.4855.996, 1988.

Cullen, H. M., Kaplan, A., Arkin, P. A., and Demenocal, P. B.: Impact of the North Atlantic Oscillation on Middle Eastern climate and streamflow, Climatic Change, 55, 315–338, https://doi.org/10.1023/A:1020518305517, 2002.

Dafka, S., Xoplaki, E., Toreti, A., Zanis, P., Tyrlis, E., Zerefos, C., and Luterbacher, J.: The Etesians: from observations to reanalysis, Climate Dynamics, 47, 1569–1585, https://doi.org/10.1007/s00382-015-2920-7, 2016.

Degroot, D., Anchukaitis, K., Bauch, M., Burnham, J., Carnegy, F., Cui, J., de Luna, K., Guzowski, P., Hambrecht, G., Huhtamaa, H., Izdebski, A., Kleemann, K., Moesswilde, E., Neupane, N., Newfield, T., Pei, Q., Xoplaki, E., and Zappia, N.: Towards a rigorous understanding of societal responses to climate change, Nature, 591, 539–550, https://doi.org/10.1038/s41586-021-03190-2, 2021.

Doms, G., Förstner, J., Heise, E., Herzog, H., Mironov, D., Raschendorfer, M., Reinhardt, T., Ritter, B., Schrodin, R., Schulz, J.-P., and Vogel, G.: A Description of the Nonhydrostatic Regional COSMO Model. Part II: Physical parameterization, Deutscher Wetterdienst, Offenbach, Germany, available at http://www.cosmo-model.org/, 2011.

Fairbanks, R., Evans, M., Rubenstone, J., Mortlock, R., Broad, K., Moore, M., and Charles, C.: Evaluating climate indices and their geochemical proxies measured in corals, Coral Reefs, 16, S93–S100, https://doi.org/10.1007/s003380050245, 1997.

Feldman, L. H.: Abba Kolon and the Founding of Rome, The Jewish Quarterly Review, 81, 239–266, http://www.jstor.org/stable/1455320, 1991.

Felis, T. and Pätzold, J.: Climate Records from Corals, pp. 11–27, Springer Berlin Heidelberg, Berlin, Heidelberg, ISBN 978-3-642-55862-7, https://doi.org/10.1007/978-3-642-55862-7_2, 2003.

Gibbons, A.: Eruption made 536 'the worst year to be alive', Science, 362, 733–734, https://doi.org/10.1126/science.362.6416.733, 2018.

Giorgetta, M. A., Jungclaus, J., Reick, C. H., Legutke, S., Bader, J., Böttinger, M., Brovkin, V., Crueger, T., Esch, M., Fieg, K., Glushak, K., Gayler, V., Haak, H., Hollweg, H.-D., Ilyina, T., Kinne, S., Kornblueh, L., Matei, D., Mauritsen, T., Mikolajewicz, U., Mueller, W., Notz, D., Pithan, F., Raddatz, T., Rast, S., Redler, R., Roeckner, E., Schmidt, H., Schnur, R., Segschneider, J., Six, K. D., Stockhause, M., Timmreck, C., Wegner, J., Widmann, H., Wieners, K.-H., Claussen, M., Marotzke, J., and Stevens, B.: Climate and carbon cycle changes from 1850 to 2100 in MPI-ESM simulations for the Coupled Model Intercomparison Project phase 5, Journal of Advances in Modeling Earth Systems, 5, 572–597, https://doi.org/10.1002/jame.20038, 2013.

Goosse, H., Renssen, H., Timmermann, A., and Bradley, R. S.: Internal and forced climate variability during the last millennium: a model-data comparison using ensemble simulations, Quaternary Science Reviews, 24, 1345–1360, https://doi.org/https://doi.org/10.1016/j.quascirev.2004.12.009, 2005.

https://doi.org/10.5194/egusphere-2026-1636
Preprint. Discussion started: 8 April 2026

Gunn, J. D.: The years without summer: Tracing AD 536 and its aftermath, BAR Publishing, https://doi.org/https://doi.org/10.30861/9781841710747, 2000.

Hartmann, E., Zhang, M., Wagner, S., Adakudlu, M., Luterbacher, J., and Xoplaki, E.: On the implementation of external forcings in a regional climate model – a sensitivity study around the Samalas volcanic eruption in the Eastern Mediterranean/Middle East, Climate of the Past, 21, 1699–1724, https://doi.org/10.5194/cp-21-1699-2025, 2025.

Helama, S., Jones, P. D., and Briffa, K. R.: Limited Late Antique cooling, Nature Geoscience, 10, 242–243, https://doi.org/10.1038/ngeo2926, 2017a.

Helama, S., Jones, P. D., and Briffa, K. R.: Dark Ages Cold Period: A literature review and directions for future research, The Holocene, 27, 1600–1606, https://doi.org/10.1177/0959683617693898, 2017b.

Helama, S., Arppe, L., Uusitalo, J., Holopainen, J., Mäkelä, H. M., Mäkinen, H., Mielikäinen, K., Nöjd, P., Sutinen, R., Taavitsainen, J.-P., Timonen, M., and Oinonen, M.: Volcanic dust veils from sixth century tree-ring isotopes linked to reduced irradiance, primary production and human health, Scientific Reports, 8, 1339, https://doi.org/10.1038/s41598-018-19760-w, 2018.

Holmgren, K., Gogou, A., Izdebski, A., Luterbacher, J., Sicre, M.-A., and Xoplaki, E.: Mediterranean Holocene climate, environment and human societies, Quaternary Science Reviews, 136, 1 – 4, https://doi.org/https://doi.org/10.1016/j.quascirev.2015.12.014, special Issue: Mediterranean Holocene Climate, Environment and Human Societies, 2016.

Ilyina, T., Six, K. D., Segschneider, J., Maier-Reimer, E., Li, H., and Núñez-Riboni, I.: Global ocean biogeochemistry model HAMOCC: Model architecture and performance as component of the MPI-Earth system model in different CMIP5 experimental realizations, Journal of Advances in Modeling Earth Systems, 5, 287–315, https://doi.org/https://doi.org/10.1029/2012MS000178, 2013.

Ingram, M., Underhill, D., and Farmer, G.: The use of documentary sources for the study of past climates, p. 180–213, Cambridge University Press, ISBN 9780521312202, 1985.

Iturbide, M., Gutiérrez, J. M., Alves, L. M., Bedia, J., Cerezo-Mota, R., Cimadevilla, E., Cofiño, A. S., Di Luca, A., Faria, S. H., Gorodetskaya, I. V., Hauser, M., Herrera, S., Hennessy, K., Hewitt, H. T., Jones, R. G., Krakovska, S., Manzanas, R., Martínez-Castro, D., Narisma, G. T., Nurhati, I. S., Pinto, I., Seneviratne, S. I., van den Hurk, B., and Vera, C. S.: An update of IPCC climate reference regions for subcontinental analysis of climate model data: definition and aggregated datasets, Earth System Science Data, 12, 2959–2970, https://doi.org/10.5194/essd-12-2959-2020, 2020.

Izdebski, A. and Mulryan, M.: Environment and Society in the Long Late Antiquity, Brill, Leiden, Niederlande, ISBN 978-90-04-39208-3, https://doi.org/10.1163/9789004392083, 2019.

Izdebski, A., Holmgren, K., Weiberg, E., Stocker, S. R., Büntgen, U., Florenzano, A., Gogou, A., Leroy, S. A., Luterbacher, J., Martrat, B., Masi, A., Mercuri, A. M., Montagna, P., Sadori, L., Schneider, A., Sicre, M.-A., Triantaphyllou, M., and Xoplaki, E.: Realising consilience: How better communication between archaeologists, historians and natural scientists can transform the study of past climate change in the Mediterranean, Quaternary Science Reviews, 136, 5 – 22, https://doi.org/https://doi.org/10.1016/j.quascirev.2015.10.038, special Issue: Mediterranean Holocene Climate, Environment and Human Societies, 2016.

Jameson, A., Schmidt, W., and Turkel, E.: Numerical solution of the Euler equations by finite volume methods using Runge Kutta time stepping schemes, https://doi.org/10.2514/6.1981-1259, 1981.

Jungclaus, J. H., Fischer, N., Haak, H., Lohmann, K., Marotzke, J., Matei, D., Mikolajewicz, U., Notz, D., and von Storch, J. S.: Characteristics of the ocean simulations in the Max Planck Institute Ocean Model (MPIOM) the ocean component of the MPI-Earth system model, Journal of Advances in Modeling Earth Systems, 5, 422–446, https://doi.org/https://doi.org/10.1002/jame.20023, 2013.

https://doi.org/10.5194/egusphere-2026-1636
Preprint. Discussion started: 8 April 2026

Jungclaus, J. H., Bard, E., Baroni, M., Braconnot, P., Cao, J., Chini, L. P., Egorova, T., Evans, M., González-Rouco, J. F., Goosse, H., Hurtt, G. C., Joos, F., Kaplan, J. O., Khodri, M., Klein Goldewijk, K., Krivova, N., LeGrande, A. N., Lorenz, S. J., Luterbacher, J., Man, W., Maycock, A. C., Meinshausen, M., Moberg, A., Muscheler, R., Nehrbass-Ahles, C., Otto-Bliesner, B. I., Phipps, S. J., Pongratz, J., Rozanov, E., Schmidt, G. A., Schmidt, H., Schmutz, W., Schurer, A., Shapiro, A. I., Sigl, M., Smerdon, J. E., Solanki, S. K., Timmreck, C., Toohey, M., Usoskin, I. G., Wagner, S., Wu, C.-J., Yeo, K. L., Zanchettin, D., Zhang, Q., and Zorita, E.: The PMIP4 contribution to CMIP6 – Part 3: The last millennium, scientific objective, and experimental design for the PMIP4 *past1000* simulations, Geoscientific Model Development, 10, 4005–4033, https://doi.org/10.5194/gmd-10-4005-2017, 2017.

Luterbacher, J., Xoplaki, E., Dietrich, D., Rickli, R., Jacobeit, J., Beck, C., Gyalistras, D., Schmutz, C., and Wanner, H.: Reconstruction of sea level pressure fields over the Eastern North Atlantic and Europe back to 1500, Climate Dynamics, 18, 545–561, https://doi.org/10.1007/s00382-001-0196-6, 2002.

Luterbacher, J., Dietrich, D., Xoplaki, E., Grosjean, M., and Wanner, H.: European Seasonal and Annual Temperature Variability, Trends, and Extremes Since 1500, Science, 303, 1499–1503, https://doi.org/10.1126/science.1093877, 2004.

Luterbacher, J., García-Herrera, R., Akcer-On, S., Allan, R., Alvarez-Castro, M.-C., Benito, G., Booth, J., Büntgen, U., Cagatay, N., Colombaroli, D., Davis, B., Esper, J., Felis, T., Fleitmann, D., Frank, D., Gallego, D., Garcia-Bustamante, E., Glaser, R., Gonzalez-Rouco, F. J., Goosse, H., Kiefer, T., Macklin, M. G., Manning, S. W., Montagna, P., Newman, L., Power, M. J., Rath, V., Ribera, P., Riemann, D., Roberts, N., Sicre, M.-A., Silenzi, S., Tinner, W., Tzedakis, P., Valero-Garcés, B., van der Schrier, G., Vannière, B., Vogt, S., Wanner, H., Werner, J. P., Willett, G., Williams, M. H., Xoplaki, E., Zerefos, C. S., and Zorita, E.: 2 - A Review of 2000 Years of Paleoclimatic Evidence in the Mediterranean, in: The Climate of the Mediterranean Region, edited by Lionello, P., pp. 87–185, Elsevier, Oxford, ISBN 978-0-12-416042-2, https://doi.org/https://doi.org/10.1016/B978-0-12-416042-2.00002-1, 2012.

Luterbacher, J., Newfield, T. P., Xoplaki, E., Nowatzki, E., Luther, N., Zhang, M., and Khelifi, N.: Past pandemics and climate variability across the Mediterranean, Euro-Mediterranean Journal for Environmental Integration, 5, 46, https://doi.org/10.1007/s41207-020-00197-5, 2020.

Mangini, A., Spötl, C., and Verdes, P.: 'Reconstruction of temperature in the Central Alps during the past 2000 yr from a δ18O stalagmite record', Earth and Planetary Science Letters, 235, 741–751, https://doi.org/https://doi.org/10.1016/j.epsl.2005.05.010, 2005.

Mann, M. E.: The Value of Multiple Proxies, Science, 297, 1481–1482, https://doi.org/10.1126/science.1074318, 2002.

Meinshausen, M., Vogel, E., Nauels, A., Lorbacher, K., Meinshausen, N., Etheridge, D. M., Fraser, P. J., Montzka, S. A., Rayner, P. J., Trudinger, C. M., Krummel, P. B., Beyerle, U., Canadell, J. G., Daniel, J. S., Enting, I. G., Law, R. M., Lunder, C. R., O'Doherty, S., Prinn, R. G., Reimann, S., Rubino, M., Velders, G. J., Vollmer, M. K., Wang, R. H., and Weiss, R.: Historical greenhouse gas concentrations for climate modelling (CMIP6), Geoscientific Model Development, 10, 2057 – 2116, https://doi.org/10.3929/ethz-b-000191830, 2017.

Moreland, J.: AD536 – BACK TO NATURE?, Acta Archaeologica, 89, 91–111, https://doi.org/https://doi.org/10.1111/j.1600-0390.2018.12194.x, 2018.

Neukom, R., Steiger, N., Gómez-Navarro, J. J., Wang, J., and Werner, J. P.: No evidence for globally coherent warm and cold periods over the preindustrial Common Era, Nature, 571, 550–554, https://doi.org/https://doi.org/10.1038/s41586-019-1401-2, 2019.

Newfield, T. P.: Mysterious and Mortiferous Clouds: The Climate Cooling and Disease Burden of Late Antiquity, Late Antique Archaeology, 12, 89 – 115, https://doi.org/https://doi.org/10.1163/22134522-12340068, 2016.

Newfield, T. P.: The Climate Downturn of 536–50, pp. 447–493, Palgrave Macmillan UK, London, ISBN 978-1-137-43020-5, https://doi.org/10.1057/978-1-137-43020-5_32, 2018.

https://doi.org/10.5194/egusphere-2026-1636
Preprint. Discussion started: 8 April 2026

Nicholson, S. E.: The ITCZ and the Seasonal Cycle over Equatorial Africa, Bulletin of the American Meteorological Society, 99, 337 – 348, https://doi.org/10.1175/BAMS-D-16-0287.1, 2018.

Pauling, A., Luterbacher, J., Casty, C., and Wanner, H.: Five hundred years of gridded high-resolution precipitation reconstructions over Europe and the connection to large-scale circulation, Climate dynamics, 26, 387–405, https://doi.org/10.1007/s00382-005-0090-8, 2006.

Peregrine, P. N.: Climate and social change at the start of the Late Antique Little Ice Age, The Holocene, 30, 1643–1648, https://doi.org/10.1177/0959683620941079, 2020.

Reick, C. H., Raddatz, T., Brovkin, V., and Gayler, V.: Representation of natural and anthropogenic land cover change in MPI-ESM, Journal of Advances in Modeling Earth Systems, 5, 459–482, https://doi.org/https://doi.org/10.1002/jame.20022, 2013.

Riechelmann, D. F. and Gouw-Bouman, M. T.: A review of climate reconstructions from terrestrial climate archives covering the first millennium AD in northwestern Europe, Quaternary Research, 91, 111–131, https://doi.org/10.1017/qua.2018.84, 2019.

Robock, A.: Volcanic eruptions and climate, Reviews of Geophysics, 38, 191–219, https://doi.org/https://doi.org/10.1029/1998RG000054, 2000.

Rockel, B., Will, A., and Hense, A.: The Regional Climate Model COSMO-CLM (CCLM), Meteorologische Zeitschrift, 17, 347–348, https://doi.org/10.1127/0941-2948/2008/0309, 2008.

Sallares, R.: The Ecology of the Ancient Greek World, Cornell University Press, 1991.

Schneck, R., Reick, C. H., and Raddatz, T.: Land contribution to natural CO2 variability on time scales of centuries, Journal of Advances in Modeling Earth Systems, 5, 354–365, https://doi.org/https://doi.org/10.1002/jame.20029, 2013.

Schulz, J.-P., Vogel, G., Becker, C., Kothe, S., Rummel, U., and Ahrens, B.: Evaluation of the ground heat flux simulated by a multi-layer land surface scheme using high-quality observations at grass land and bare soil, Meteorologische Zeitschrift, 25, 607–620, https://doi.org/10.1127/metz/2016/0537, 2016.

Schättler, U. and Blahak, U.: A Description of the Nonhydrostatic Regional COSMO-Model. Part V: Preprocessing: Initial and Boundary Data for the COSMO-Model, Deutscher Wetterdienst, Offenbach, Germany, available at http://www.cosmo-model.org/, 2017.

Shi, F., Sun, C., Guion, A., Yin, Q., Zhao, S., Liu, T., and Guo, Z.: Roman Warm Period and Late Antique Little Ice Age in an Earth System Model Large Ensemble, Journal of Geophysical Research: Atmospheres, 127, e2021JD035 832, https://doi.org/https://doi.org/10.1029/2021JD035832, e2021JD035832 2021JD035832, 2022.

Sigl, M., Winstrup, M., McConnell, J. R., Welten, K. C., Plunkett, G., Ludlow, F., Büntgen, U., Caffee, M., Chellman, N., Dahl-Jensen, D., Fischer, H., Kipfstuhl, S., Kostick, C., Maselli, O., Mekhaldi, F., Mulvaney, R., Muscheler, R., Pasteris, D., Pilcher, J., Salzer, M., Schüpbach, S., Steffensen, J., Vinther, B., and Woodruff, T.: Timing and climate forcing of volcanic eruptions for the past 2,500 years, Nature, 523, 543–549, https://doi.org/10.1038/nature14565, 2015.

Simpson, I. R., Seager, R., Shaw, T. A., and Ting, M.: Mediterranean Summer Climate and the Importance of Middle East Topography, Journal of Climate, 28, 1977 – 1996, https://doi.org/10.1175/JCLI-D-14-00298.1, 2015.

Smerdon, J., Luterbacher, J., Phipps, S., Anchukaitis, K., Ault, T., Coats, S., Cobb, K., Cook, B., Colose, C., Felis, T., Gallant, A., Jungclaus, J., Konecky, B., LeGrande, A., Lewis, S., Lopatka, A., Man, W., Mankin, J., Maxwell, J., and Xoplaki, E.: Comparing proxy and model estimates of hydroclimate variability and change over the Common Era, Climate of the Past, 13, 1851–1900, https://doi.org/10.5194/cp-13-1851-2017, 2017.

Stevens, B., Giorgetta, M., Esch, M., Mauritsen, T., Crueger, T., Rast, S., Salzmann, M., Schmidt, H., Bader, J., Block, K., Brokopf, R., Fast, I., Kinne, S., Kornblueh, L., Lohmann, U., Pincus, R., Reichler, T., and Roeckner, E.: Atmospheric component of the MPI-M Earth System Model: ECHAM6, Journal of Advances in Modeling Earth Systems, 5, 146–172, https://doi.org/https://doi.org/10.1002/jame.20015, 2013.

https://doi.org/10.5194/egusphere-2026-1636
Preprint. Discussion started: 8 April 2026

Swingedouw, D., Mignot, J., Ortega, P., Khodri, M., Menegoz, M., Cassou, C., and Hanquiez, V.: Impact of explosive volcanic eruptions on the main climate variability modes, Global and Planetary Change, 150, 24–45, https://doi.org/https://doi.org/10.1016/j.gloplacha.2017.01.006, 2017.

Thornes, J. B., López-Bermúdez, F., and Woodward, J. C.: The Physical Geography of the Mediterranean, chap. Hydrology, river regimes, and sediment yield, pp. 229–253, Oxford University Press, Oxford, 2009.

Tiedtke, M.: Parameterization of Cumulus Convection in Large-Scale Models, pp. 375–431, Springer Netherlands, Dordrecht, ISBN 978-94-009-3041-4, https://doi.org/10.1007/978-94-009-3041-4_9, 1988.

Toohey, M. and Sigl, M.: Volcanic stratospheric sulphur injections and aerosol optical depth from 500 BCE to 1900 CE, Earth System Science Data, 9, 809–831, https://doi.org/doi:10.5194/essd-9-809-2017, 2017.

Toohey, M., Stevens, B., Schmidt, H., and Timmreck, C.: Easy Volcanic Aerosol (EVA v1.0): an idealized forcing generator for climate simulations, Geoscientific Model Development, 9, 4049–4070, https://doi.org/10.5194/gmd-9-4049-2016, 2016.

Turney, C. S. M., McGregor, H. V., Francus, P., Abram, N., Evans, M. N., Goosse, H., von Gunten, L., Kaufman, D., Linderholm, H., Loutre, M.-F., and Neukom, R.: Introduction to the special issue "Climate of the past 2000 years: regional and trans-regional syntheses", Climate of the Past, 15, 611–615, https://doi.org/10.5194/cp-15-611-2019, 2019.

Tyrlis, E., Lelieveld, J., and Steil, B.: The summer circulation over the eastern Mediterranean and the Middle East: influence of the South Asian monsoon, Climate Dynamics, 40, 1103–1123, https://doi.org/10.1007/s00382-012-1528-4, 2013.

Ulbrich, U., Lionello, P., Belušić, D., Jacobeit, J., Knippertz, P., Kuglitsch, F. G., Leckebusch, G. C., Luterbacher, J., Maugeri, M., Maheras, P., Nissen, K. M., Pavan, V., Pinto, J. G., Saaroni, H., Seubert, S., Toreti, A., Xoplaki, E., and Ziv, B.: 5 - Climate of the Mediterranean: Synoptic Patterns, Temperature, Precipitation, Winds, and Their Extremes, in: The Climate of the Mediterranean Region, edited by Lionello, P., pp. 301–346, Elsevier, Oxford, ISBN 978-0-12-416042-2, https://doi.org/https://doi.org/10.1016/B978-0-12-416042-2.00005-7, 2012.

Valler, V., Franke, J., Brugnara, Y., Samakinwa, E., Hand, R., Lundstad, E., Burgdorf, A.-M., Lipfert, L., Friedman, A. R., and Brönnimann, S.: ModE-RA: a global monthly paleo-reanalysis of the modern era 1421 to 2008, Scientific Data, 11, 36, https://doi.org/10.1038/s41597-023-02733-8, 2024.

van Dijk, E., Jungclaus, J., Lorenz, S., Timmreck, C., and Krüger, K.: Was there a volcanic-induced long-lasting cooling over the Northern Hemisphere in the mid-6th–7th century?, Climate of the Past, 18, 1601–1623, https://doi.org/10.5194/cp-18-1601-2022, 2022.

van Dijk, E., Mørkestøl Gundersen, I., de Bode, A., Høeg, H., Loftsgarden, K., Iversen, F., Timmreck, C., Jungclaus, J., and Krüger, K.: Climatic and societal impacts in Scandinavia following the 536 and 540 CE volcanic double event, Climate of the Past, 19, 357–398, https://doi.org/10.5194/cp-19-357-2023, 2023.

Wilson, J. A.: The culture of Ancient Egypt, University of Chicago Press, https://doi.org/10.7208/chicago/9780226148229.001.0001, 1956.

Xoplaki, E.: Climate variability over the Mediterranean, Ph.D. thesis, University of Bern, Switzerland, 2002.

Xoplaki, E., Luterbacher, J., Wagner, S., Zorita, E., Fleitmann, D., Preiser-Kapeller, J., Sargent, A. M., White, S., Toreti, A., Haldon, J. F., Mordechai, L., Bozkurt, D., Akçer-Ön, S., and Izdebski, A.: Modelling climate and societal resilience in the Eastern Mediterranean in the last millennium, Human Ecology, 46, 363–379, https://doi.org/10.1007/s10745-018-9995-9, 2018.

Xoplaki, E., Luterbacher, J., Luther, N., Behr, L., Wagner, S., Jungclaus, J., Zorita, E., Toreti, A., Fleitmann, D., Izdebski, A., and Bloomfield, K.: Hydrological Changes in Late Antiquity: Spatio-Temporal Characteristics and Socio-Economic Impacts in the Eastern Mediterranean, pp. 533–560, Springer International Publishing, Cham, ISBN 978-3-030-81103-7, https://doi.org/10.1007/978-3-030-81103-7_18, 2021.

https://doi.org/10.5194/egusphere-2026-1636
Preprint. Discussion started: 8 April 2026

670 Zanchettin, D., Timmreck, C., Toohey, M., Jungclaus, J. H., Bittner, M., Lorenz, S. J., and Rubino, A.: Clarifying the Relative Role of Forcing Uncertainties and Initial-Condition Unknowns in Spreading the Climate Response to Volcanic Eruptions, Geophysical Research Letters, 46, 1602–1611, https://doi.org/https://doi.org/10.1029/2018GL081018, 2019.